

Automatic mapping and spatial analysis of high spatial resolution closed terrain depressions and mounds on martian landscapes

E. Pardo-Igúzquiza ^{a,*}, P.A. Dowd ^b, R. Naor ^{c,d}

^a Instituto Geológico y Minero de España (IGME), Ríos Rosas 23, 28003 Madrid, Spain

^b Faculty of Engineering, Computer and Mathematical Sciences, The University of Adelaide, Australia

^c The department of Earth and Planetary Sciences, Weizmann Institute of Science, PO Box 26, Rehovot 7610001, Israel

^d Geological Survey of Israel, 32 Yesha'ayahu Leibowitz, Jerusalem 9692100, Israel

ARTICLE INFO

Keywords:

Mars
Sinks
Mounds
Digital elevation models
HiRISE
Aeolian terrain
Volcanic terrain
Hydrated terrain
Cratered terrain
Reticulate terrain
Sublimated terrain

ABSTRACT

The purpose of this paper is to illustrate a methodology for the automatic mapping and spatial analysis of high spatial resolution (metric scale) closed depressions and mounds on Mars landscapes. The proposed automatic procedure requires only a digital elevation model, a sink-filling algorithm and a basic map algebra operation all of which are available in the most commonly used Geographical Information Systems. Six high spatial resolution (1 m to 2 m) digital elevation models obtained from images of the High-Resolution Imaging Science Experiment (HiRISE) were selected as representatives of various Martian landscapes representing hypothesized aeolian, volcanic, hydrated, cratered, reticulate and sublimated terrains. This is not an exhaustive list of landscapes but it is representative of the variety of Martian landscapes. Metric spatial-scale closed depressions and mounds are commonly distributed in all the landscapes selected for this study and closed terrain depressions cover, on average, 25% of the Martian surface. Most closed depressions are small and shallow and have a complex shape. The area covered by mounds is more variable and is up to 36% in reticulate terrain and 43% in volcanic terrain. Again, most mounds are small, low and have complex shapes. For sublimated terrains the percentage covered by depressions, in the form of radiating araneiform channels, is equal to the percentage of mounds (material accumulated between the channels). Size distribution analysis reveals the fractal character of both closed depressions and mounds with the emergence of two main groups of landscapes. One group characterizes a detached geomorphology (aeolian and sublimated terrains), and the other group characterizes a connected geomorphology (volcanic, impact craters and reticulate terrain). The hydrated terrain is intermediate between the two main groups perhaps because of its plastic rheology. The proposed methodology is completely general and can be applied to any digital elevation model. The mapping and morphometric analysis of closed terrain depressions and mounds can assist planetary geologists in the mapping and interpretation of geological and geomorphological units and in the inference of geological processes.

1. Introduction

There is significant interest in detecting depressions (for example, impact craters) and mounds (for example, volcanic cones) on Mars and two approaches have been used to do so: methods based on satellite imagery and methods based on digital elevation models (DEMs). The methods based on satellite imagery range from visual inspection and expert interpretation of images to automatic methods based on computational algorithms (Jin and Zhang, 2014). Global Martian DEMs have been obtained from the Mars Orbiter Laser Altimeter (MOLA) onboard the Mars Global Surveyor. Photogrammatic methods have been

used to obtain local high-resolution DEMs by using two images of the same area on the ground taken from different angles to provide a stereopair (Hepburn et al., 2019). Ever since Martian DEMs were available, they have been used to map depressions and mounds by using pit templates (Trier and Pilø, 2012) or morphometric parameters (Pozzobon et al., 2019). None of these procedures are truly automatic but they are supervised and semi-automatic. Earth DEMs, on the other hand, have been extensively used in hydrology, particularly for delineating drainage networks and watersheds of river basins (Arnold, 2010). Pits were considered a nuisance in the estimation of drainage networks and a lot of work has been in establishing algorithms to remove pits, primarily

* Corresponding author.

E-mail address: e.pardo@igme.es (E. Pardo-Igúzquiza).

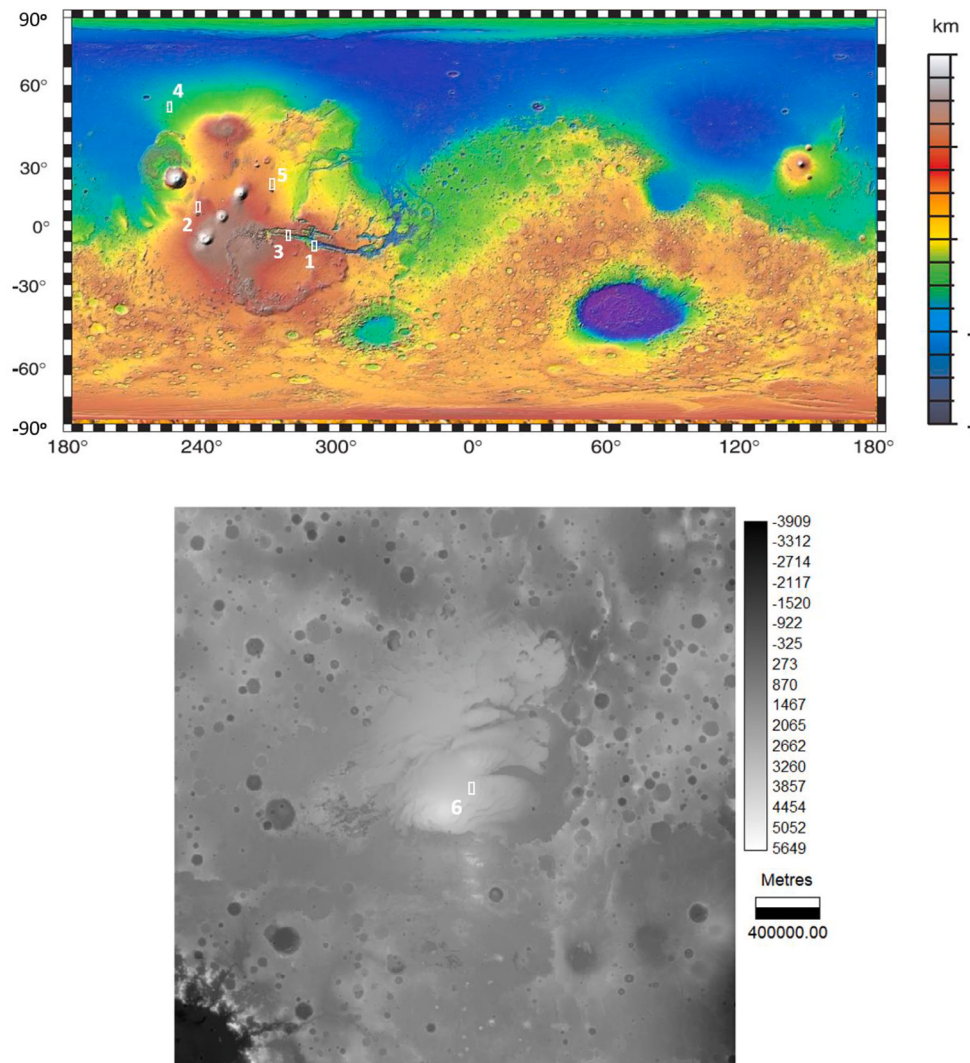


Fig. 1. The white squares show the six test sites used in this paper to study terrain closed depressions and mounds on Martian landscapes: (1) Aeolian terrain in South Melas Chasma, (2) Volcanic terrain in the Tharsis region, (3) Hydrated terrain inside Ius Chasma, (4) Cratered terrain, (5) Reticulate terrain and (6) Sublimated terrain in the layered bands of the Southern polar cap. Mars MGS MOLA Global Colour Shaded Relief from the USGS Astrogeology Science Centre, Goddard Space Flight Centre, NASA and digital elevation model of the Southern Pole.

by filling them. The seminal [Jenson and Domingue \(1988\)](#) paper on removing pits from DEMs proposed filling depressions for hydrology routing. However, the procedure is computationally intensive and faster methods were proposed, among others, by [Planchon and Darboux \(2001\)](#), [Wang and Liu \(2006\)](#), and [Yong-He et al. \(2009\)](#). [Pardo-Igúzquiza et al. \(2013\)](#), and independently ([Launspach, 2013](#)), proposed the mapping of depressions using the map algebra difference between the raw DEM and the pit-free DEM and the algorithm was used for the morphometric analysis of dolines ([Pardo-Igúzquiza et al., 2016](#)). [Pardo-Igúzquiza et al. \(2014\)](#) suggest the use of the same algorithm, with a simple adaptation, to map mounds: apply the same method but with the sign reversed (i.e., altitudes multiplied by minus one) and they applied it to map karst mounds. The procedure for mapping depressions has been used to map large-scale depressions on Mars using MOLA DEMs ([Pardo-Igúzquiza and Dowd, 2020a](#)). In this paper we have extended the method in two senses, a method for mapping mounds on Mars and the use of high resolution DEMs from HiRISE stereo-pairs, i.e., mapping metric spatial-scale depressions and mounds on Martian landscapes. The method is completely automatic and unsupervised as opposed to the alternatives.

Metric spatial-scale depressions occur extensively on Earth across lithologies, climates and a variety of origin processes: dissolution, subsidence, collapse, meteorite impact, explosive volcanism, suffusion, ice melting, erosion and weathering. The mapping of metric spatial-scale depressions can be extended to other planets and, together with other

types of data, will assist planetary scientists in the interpretation of geological surfaces and processes on these planets, in this case Mars. Thus, the study of planetary depressions and mounds is a remote sensing tool in which surface expression is used to study subsurface process and constraining subsurface properties. By forming such a linkage the study of these morphologies has the potential to add constraints on the planet's history (e.g., climate, hydrology...). Closed terrain depressions, which are typical geomorphological features on Earth and Mars, have the property of scale invariance ([Dodds and Rothman, 2000](#)). On the kilometric-scale, very large closed depressions (e.g., tectonic basins) are found on Earth ([Pardo-Igúzquiza and Dowd, 2020a](#)) and on Mars ([Spencer and Fanale, 1990](#); [Davis et al., 1995](#); [Pardo-Igúzquiza and Dowd, 2020b](#)). On the metric spatial-scale of metres to tens of metres, closed depressions are found on Earth in carbonate terrains ([Sauro, 2003, 2019](#)), gypsum terrains ([Klimchouk et al., 1996](#)), evaporites ([Gustavson et al., 1982](#)), clays ([Ferreira and Boulet, 1996](#)), loess deposits ([Gillijns et al., 2005](#)), siliciclastic rocks ([Brock-Hon et al., 2019](#)), ultramafic rocks ([Jeanpert et al., 2016](#)) and volcanic rocks ([Watson, 1986](#)) among others. These closed depressions are the result of the processes of dissolution, subsidence, suffusion, collapse phenomena, wind deflation, creation of barriers and a combination of these processes (polygenic closed depressions). Impact craters are a type of closed terrain depression that is not very frequent on Earth because of the effects of erosion and plate tectonics. On Mars, however, they are the most typical type of depression especially in the Southern Hemisphere

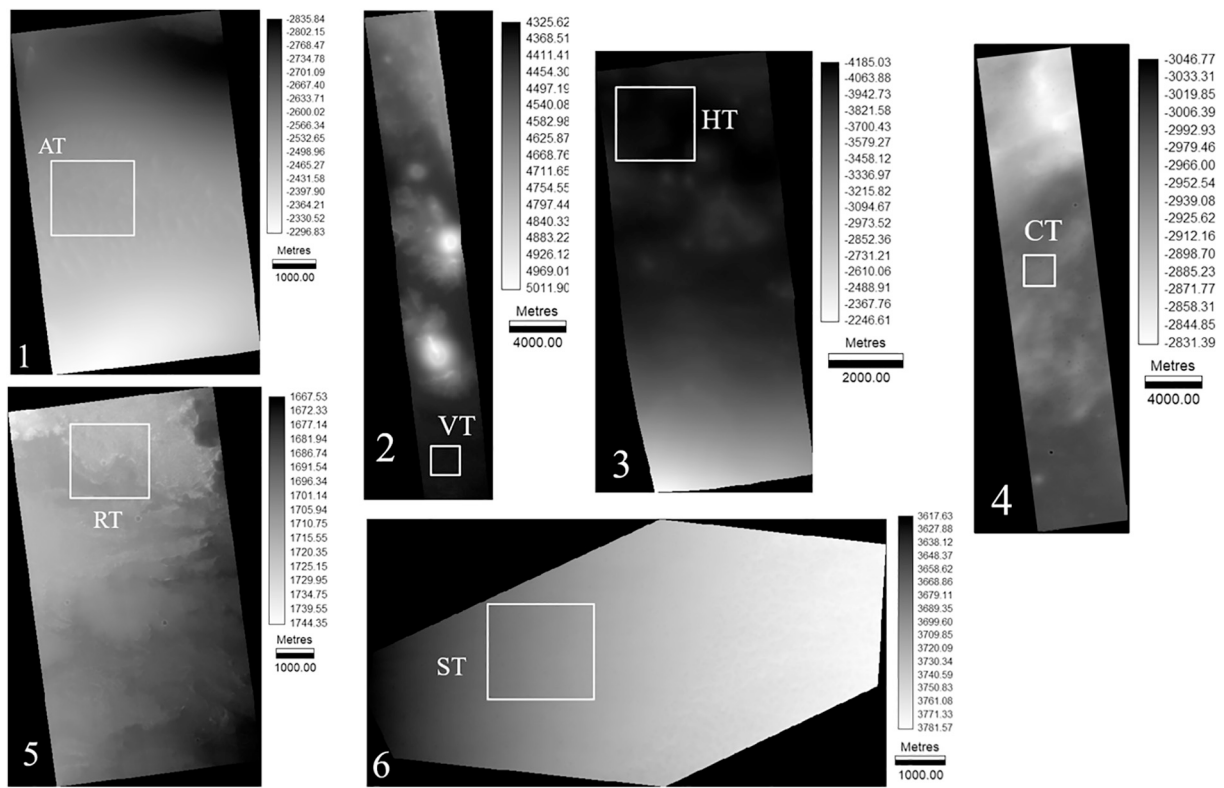


Fig. 2. Digital elevation models from HiRISE images (1) ESP_060729_1670 for aeolian terrain. (2) PSP_008262_1855 for volcanic terrain. (3) ESP_041121_1725 for hydrated terrain. (4) ESP_018007_2305 for cratered terrain. (5) ESP_025152_1945 for reticulate terrain and (6) ESP_013990_0930 for sublimated terrain. The digital elevation models are calculated from these images and their corresponding stereo-pairs. The white squares are the pilot sites used for the analysis and, in all cases, they represent a terrain area of 4 km × 4 km.

(Barlow and Bradley, 1990; Stuart and Hynek, 2012, 2014). The focus of the work presented in this paper is the spatial analysis of metric spatial-scale closed depressions on Mars, that is, closed depressions in the range of a few metres to tens of metres. As shown in this paper, at the metric spatial-scale the preponderance of impact crater depressions on Mars (Daubar et al., 2013) is not so evident even though, on average, 25% of the landscapes are covered by closed depressions. On Mars, as on Earth, many processes generate closed terrain depressions. Closed depressions on Mars have been attributed to a range of processes including dissolution resulting in karst landscapes in evaporites (Baioni et al., 2009; Baioni and Wezel, 2010; Baioni et al., 2017; Parenti et al., 2020), volcanic craters, calderas and collapsed pingos (Graettinger et al., 2017), ice depressions (Buczkowski, 2007) and scalloped depressions caused by the sublimation of ground ice (Tognetti, 2019).

Mounds are also typical geomorphic features of Earth and Mars and have the property of topographic scale invariance (Hallet, 1990; Dodds and Rothman, 2000). The work presented here introduces the concept of mapping and analysing “closed mounds” – mounds that, if topography was inverted, would be mapped as closed depressions. The way that these closed mounds are mapped allows a rim to be calculated for them and thus their heights can be calculated with respect to their rims. Thus, closed mounds and mounds are taken as synonymous. The proposed procedure is able to detect peaks inside depressions (e.g., the central peak of an impact crater) and depressions inside mounds (e.g., a volcanic vent or an impact crater on a volcanic cone) provided those features are larger than the resolution of the DEM and smaller than the dimensions of the DEM.

Typical mounds on a Martian landscape may be related to ancient sand dunes (Banham et al., 2018) or may have resulted from recent aeolian processes (Hobbs et al., 2010). On Mars, there are also sedimentary mounds on Mars (Kite et al., 2016), periglacial mounds in the form of ice-dust mounds or pingos (Soare et al., 2013), mounds related

to mud volcanism (Farrand et al., 2005; Oehler and Allen, 2010; Pondonelli et al., 2011; Komatsu et al., 2016; Hemmi and Miyamoto, 2018; Brož et al., 2019), mud diapirs (Rodríguez et al., 2007), volcanic cones (Bruno et al., 2006; Brož et al., 2015, 2017; Dapremont and Wray, 2021), tumuli (Baloga et al., 2007; De Toffoli et al., 2018; Diniega et al., 2018), lava domes from igneous volcanism (Rampney et al., 2007), spring mounds (Essefi et al., 2014) and volcanic ridges (Hiesinger and Head III, 2003). In addition, mounds can be generated by erosion processes, such as wind erosion of outcropping evaporitic domes (Baioni and Wezel, 2010) or erosion by outflow channels (Rodríguez et al., 2013). In this sense, many mesas and buttes on the Martian landscape are the remains of eroded topography (Anderson and Bell III, 2010). There are also mounds related to mass movement (Phillips et al., 2007). Tectonic processes have been proposed for kilometric-scale mounds (Oehler and Allen, 2012) and they may also explain some metric-scale mounds.

The following sections cover the automatic mapping of all closed depressions and mounds at the metric spatial-scale from digital elevation models derived from high-resolution HiRISE images of selected Mars landscapes and the morphometric analysis of these terrain depressions and mounds. Maps of metric spatial-scale morphologies can assist planetary geologists in their interpretation of Martian geological surfaces and geological processes by estimating the morphometric parameters of depressions and mounds and, for example, comparing them with Earth analogues. The intention here is not to provide an exhaustive analysis of each type of Mars landscape, but rather to illustrate of the potential of the proposed methodology for identifying and delineating closed depressions and mounds on Martian landscapes at the metric spatial-scale. For each particular test site, the methodology can be integrated with other types of information available to planetary geologists to provide a better informed and more complete interpretation.

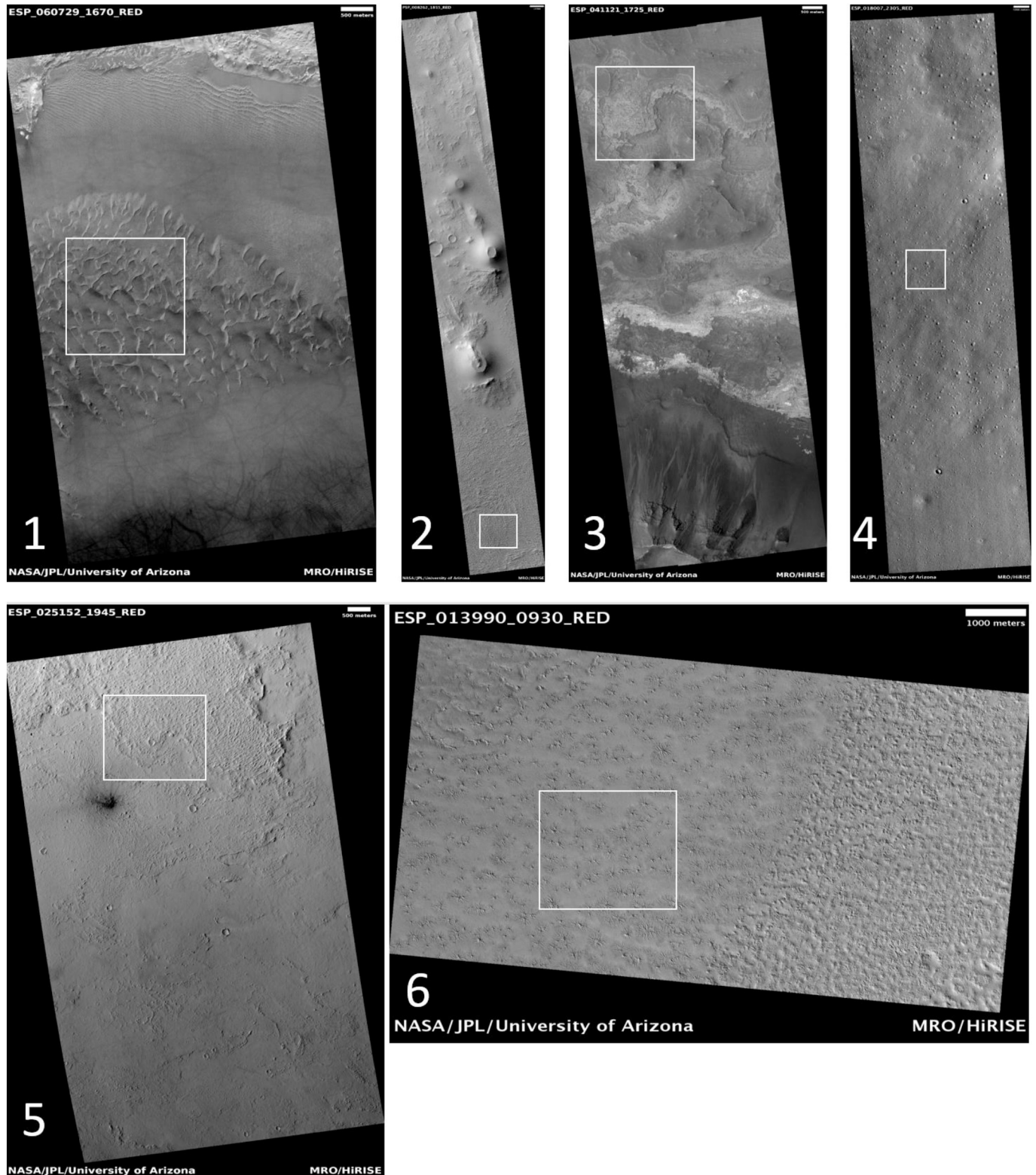


Fig. 3. HiRISE images (1) ESP_060729_1670 for aeolian terrain. (2) PSP_008262_1855 for volcanic terrain. (3) ESP_041121_1725 for hydrated terrain. (4) ESP_018007_2305 for cratered terrain. (5) ESP_025152_1945 for reticulate terrain and (6) ESP_013990_0930 for sublimated terrain.

2. Data and methods

2.1. Data

The digital elevation models (DEMs) used in this paper, widely

referred to as HiRISE DTMs (HiRISE digital terrain models), were obtained from the images gathered by the High Resolution Imaging Science Experiment (HiRISE) cameras (McEwen et al., 2010) on board the NASA Mars Reconnaissance Orbiter spacecraft (Graf et al., 2005) and were downloaded from the HiRISE internet site (<https://www.uahirise.org/>).

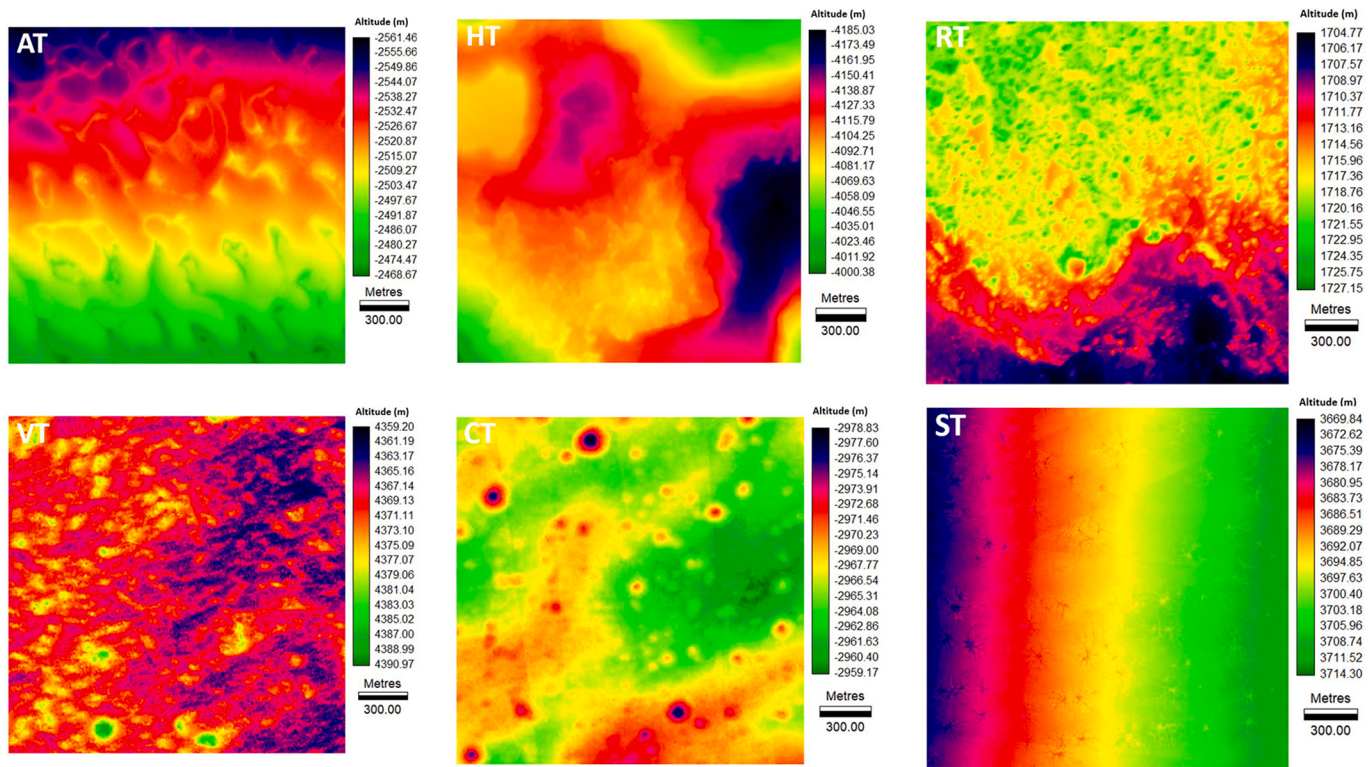


Fig. 4. Digital elevation model (DEM) of each of the pilot sites. Aeolian terrain (AT), volcanic terrain (VT), hydrated terrain (HT), cratered terrain (CT), reticulate terrain (RT) and sublimated terrain (ST). The size of each square is 4 km × 4 km in all cases and the colour legend represents altitude in metres.

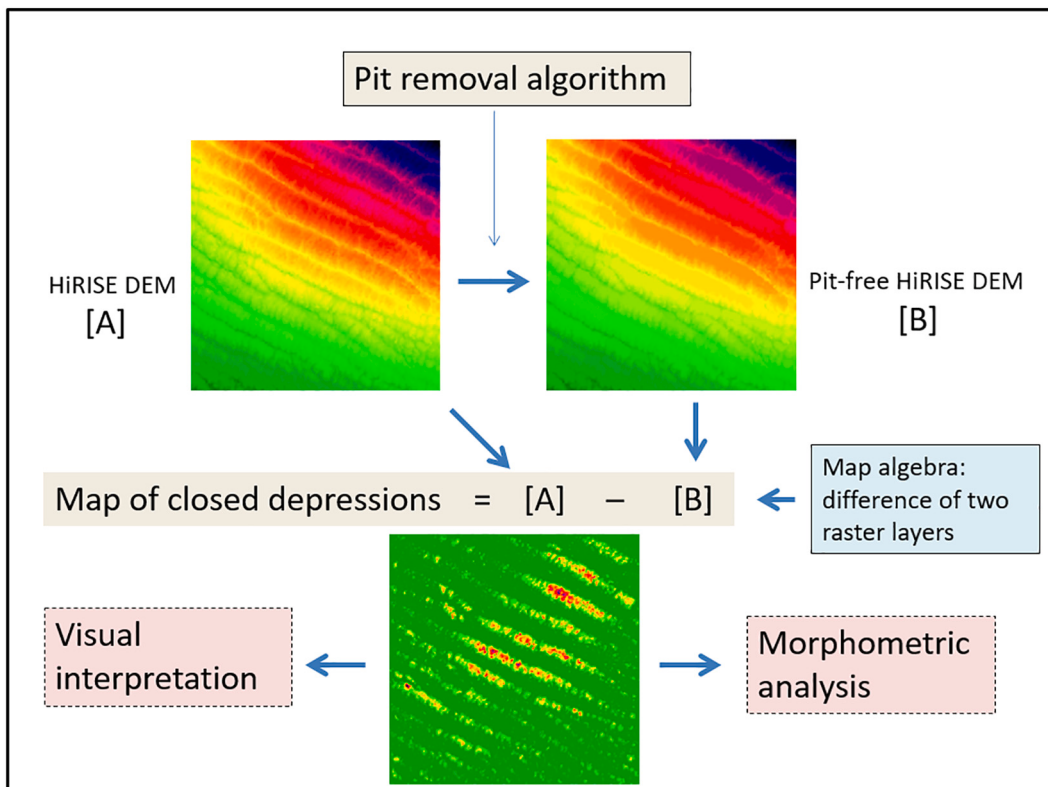


Fig. 5. Flow chart for identifying and delineating closed ground depressions. An efficient pit removal algorithm is applied to a digital elevation model [A] to obtain a pit-free DEM [B]. The map of closed depressions is the difference (map algebra operation) between layer [A] and layer [B].

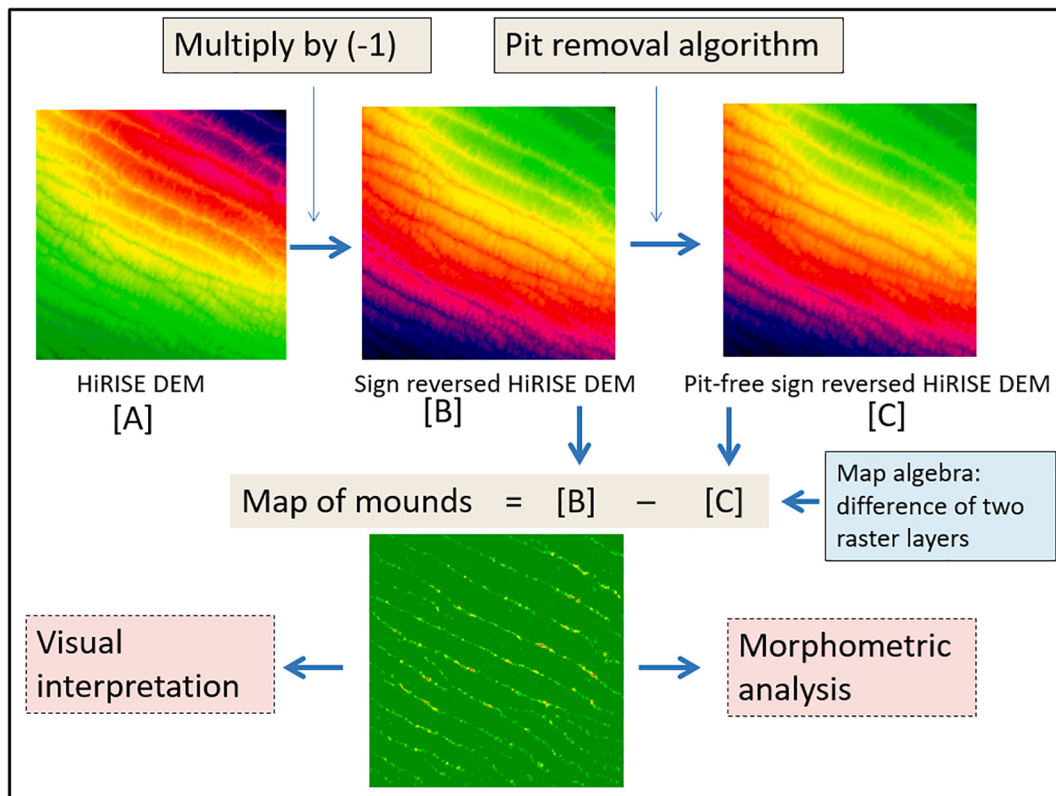


Fig. 6. Flow chart for identifying and delineating terrain mounds. The procedure for mapping mounds is the same as that for mapping closed depressions (Fig. 1) except that it is applied to the DEM after reversing the sign of its values (multiplication by -1). The map of mounds is the difference (map algebra operation) between layer [B] and layer [C].

org/dtm/). In general, the spatial resolution of the DEM is 1 m. That is, each pixel represents the mean altitude of a square of the terrain of side length 1 m. However, in some cases the spatial resolution is 2 m. The DEMs are derived from high resolution stereo-pair images (Kirk et al., 2008; Kim et al., 2013) and they have an altimetric uncertainty of a few tens of centimetres (McEwen et al., 2010). HiRISE data are being used to create the most accurate local topographic maps of Mars and are contributing significantly to our knowledge of Martian geology at the local scale.

Six HiRISE derived DEMs were selected for this study, the locations of which are shown as white squares in the Mars global topographic map in Fig. 1. The six DEMs are shown in Fig. 2. The six HiRISE images are shown in Fig. 3 to assist in understanding the appearance of the topographic features in the DEMs. A test site was selected for each HiRISE DEM and these are shown as white squares in Fig. 2. Each DEM represents a surface of $4\text{ km} \times 4\text{ km}$ in terrain units, and each comprises a raster image of 2000 rows and 2000 columns for the 1 m resolution DEMs (AT, HT, RT and ST in Fig. 2) and raster images of 1000 rows and 1000 columns for the 2 m resolution DEMs (VT and CT in Fig. 2). The DEMs of the test sites are shown in Fig. 3 for aeolian terrain (AT), volcanic terrain (VC), hydrated terrain (HT), cratered terrain (CT), reticulate terrain (RT) and sublimated terrain (ST). The six terrains are named after the most distinctive, but no the unique, morphologic process that shaped the examined landscape. This is considered to be a representative, but not exhaustive, selection of Martian landscapes for mapping and analysing metric-scale closed depressions and mounds. The selection of the sites was arbitrary although the intention was to use a wide variety of different origin-related terrains and it so happens that such a group is located around the Tharsis dome. This does not imply a bias in the results and, for example, a field of dunes (Aeolian process) can also be found in the northern lowlands or in the southern highlands. The procedure can be applied to any DEM for any part of Mars. The

differences between the textures of the selected landscapes are evident in Fig. 4. Test site 1 (Fig. 1) is centred at a longitude of 289.17° east and a latitude 13.08° south, in the southern part of the Melas Chasma in Valles Marineris. This test site was selected as representative of aeolian terrain (AT), that is, with a landscape sculpted by the wind. It should be noted that despite the thin Martian atmosphere, the wind on Mars is a more powerful geomorphic agent than it is on Earth (McCauley, 1973). Test site 2 (Fig. 1) is centred at a longitude of 237.02° east and a latitude 5.64° north, in the northern part of Ulysses Tholus and close to Ulysses Fossae in the Tharsis dome. This test site was selected as being representative of volcanic terrain (VT), that is, with a landscape sculpted by volcanic processes. Test site 3 (Fig. 1) is centred at a longitude of 276.98° east and a latitude 7.24° south, inside Ius Chasma in Valles Marineris. This test site was selected as representative of hydrated terrain (HT), a light-toned landscape representative of diapiric-like processes. Test site 4 (Fig. 1) is centred at a longitude of 219.21° east and a latitude 49.95° north, in Lycus Sulci northwest of Olympus Mons. This test site is selected as representative of cratered terrain (CT), that is, a landscape representative of impact cratering without any resurfacing by other processes. Test site 5 (Fig. 1) is centred at a longitude of 268.87° east and a latitude 14.49° north, on the northern flank of the Tharsis Tholus volcano. This test site was selected as being representative of reticulate terrains (RT), that is, a landscape representative of polygenetic processes. Test site 6 (Fig. 1) is centred at a longitude of 127.40° east and a latitude 87.01° south, in the Southern Polar cap. This test site was selected as representative of sublimated terrain (ST), that is, a landscape representative of a CO_2 ice sublimation process.

2.2. Identification and delineation of terrain closed depressions

As the spatial resolution of the HiRISE DEM is 1 m (or 2 m in some cases), the study presented here is limited to closed depressions equal to

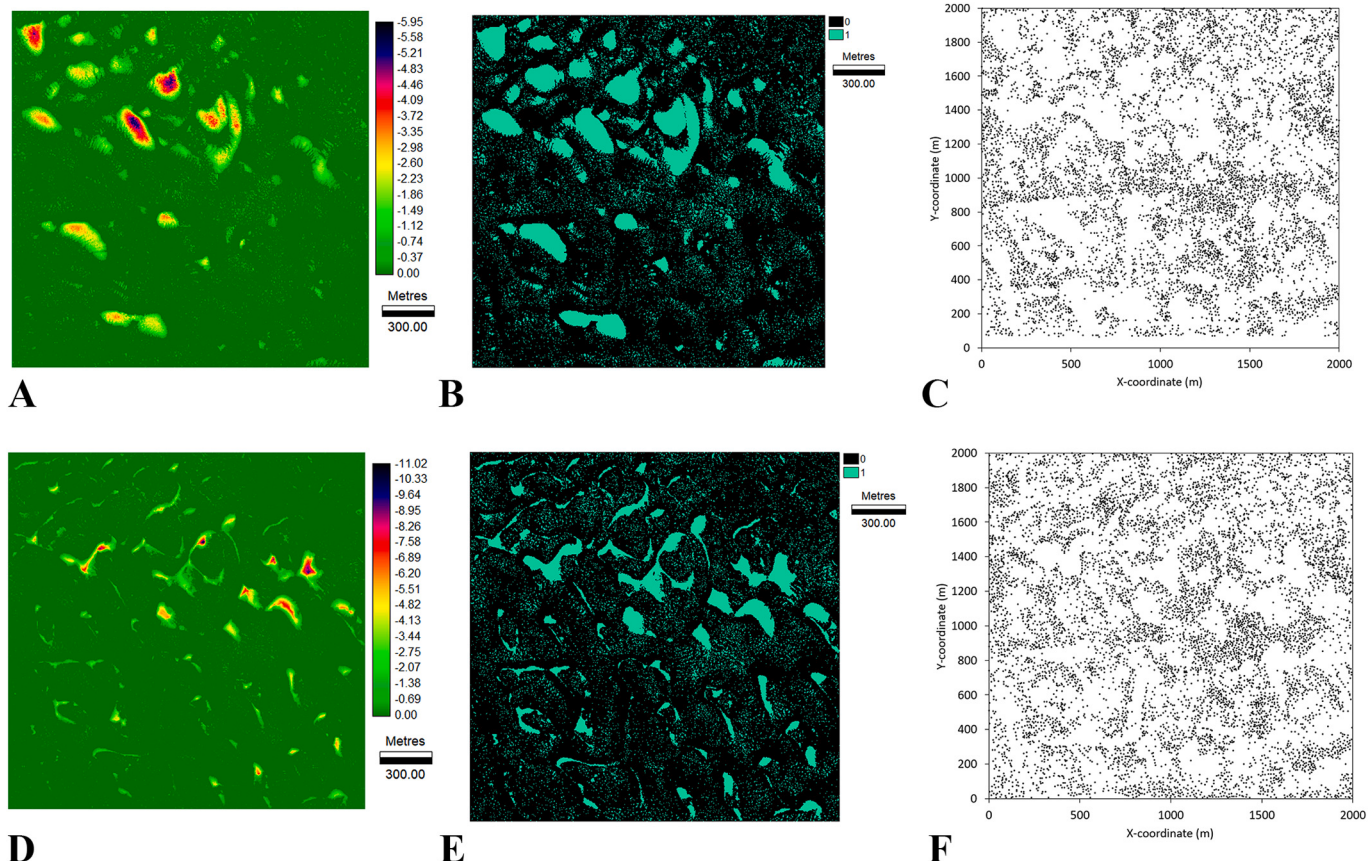


Fig. 7. Aeolian terrain (AT). A. Closed terrain depressions. B. Binary map of closed terrain depressions. C. Point map of the centroids of closed terrain depressions. D. Terrain mounds. E. Binary map of mounds. F. Point map of the centroids of mounds.

Table 1

Relief range statistics obtained from the DEM and statistics of closed terrain depressions (maximum depth, percentage of depressions in the study areas and percentage of depressions larger than 16 m^2 in the study areas) and mounds (maximum altitude, percentage of mounds in the study areas and percentage of mounds larger than 16 m^2 in the study areas). The value of 16 m^2 was chosen arbitrarily as a depression with 16 cells in the 1 m spatial resolution DEMs and 4 cells in the 2 m spatial resolution DEMs. All the DEMs have a spatial resolution of 1 m except those marked with an asterisk (*), which have a spatial resolution of 2 m.

| Terrain type (test sites) | Depressions (Ds) | | | | Mounds (Ms) | | | |
|---------------------------|----------------------|-------------------|------------------|------------------------|----------------------|----------------------|------------------|------------------------|
| | Relief amplitude (m) | Maximum depth (m) | Area with Ds (%) | Area with large Ds (%) | Relief amplitude (m) | Maximum altitude (m) | Area with Ms (%) | Area with large Ms (%) |
| Aeolian | 93 | -5.95 | 18.01 | 15.83 | 93 | 11.02 | 14.24 | 11.95 |
| Volcanic (*) | 32 | -6.01 | 34.42 | 34.03 | 32 | 18.51 | 42.82 | 42.39 |
| Hydrated | 185 | -28.55 | 22.13 | 20.88 | 185 | 15.30 | 10.91 | 9.45 |
| Cratered (*) | 20 | -10.92 | 25.37 | 24.94 | 20 | 1.70 | 17.13 | 16.75 |
| Reticulate | 22 | -2.80 | 24.04 | 23.74 | 22 | 7.73 | 36.33 | 36.15 |
| Sublimated | 44 | -5.39 | 27.74 | 19.27 | 44 | 4.46 | 27.06 | 18.74 |

1 pixel-scale depression, or greater than, 1 m (or 2 m). As the size of the test images is $4 \text{ km} \times 4 \text{ km}$, it is not possible to map depressions larger than this image size. The method for identifying and delineating terrain depressions was initially proposed in Pardo-Igúzquiza et al. (2013) and was applied to the mapping of kilometric-scale closed depressions, using MOLA DEMs, in Pardo-Igúzquiza and Dowd (2020b). In the work presented here, the methodology is applied to mapping metric spatial-scale closed depressions using HiRISE DEMs and to the identification and delineation of metric-scale mounds. The methodology for identifying and delineating closed terrain depressions is summarized in Fig. 5. The proposed approach is based on a simple but powerful idea that only requires a DEM. In surface hydrology the most common applications of DEMs are the automatic derivation of drainage networks and the delineation of watersheds (Jenson, 1991). In these applications, the first step is to remove spurious terrain pits to generate pit-free DEMs. Many of

these algorithms are based on the method of Jenson and Domingue (1988) which has been implemented in commercial software packages, such as the “pit removal” command in IDRISI (Clark Labs, 2000) or in ArcGIS by using the “sink” and “fill” commands (ESRI, 2011). Identical results can be obtained by using open access GIS, such as QGIS (QGIS Development Team, 2020), which uses the “fill sinks” command (Wang and Liu, 2006), and SAGA (Conrad et al., 2015). Once a pit-free DEM has been generated, a map of depressions is easily obtained as the map algebra operation of the raster difference between the original DEM and the pit-free DEM. On Earth the procedure has been applied to high relief karst systems (Pardo-Igúzquiza et al., 2014, 2016) and it has been validated in the field. It has also been observed that it works well for the natural slopes found in these mountainous terrains.

It should be noted that the map depressions is a raster image with the same spatial resolution as the DEM and shows the depth of each

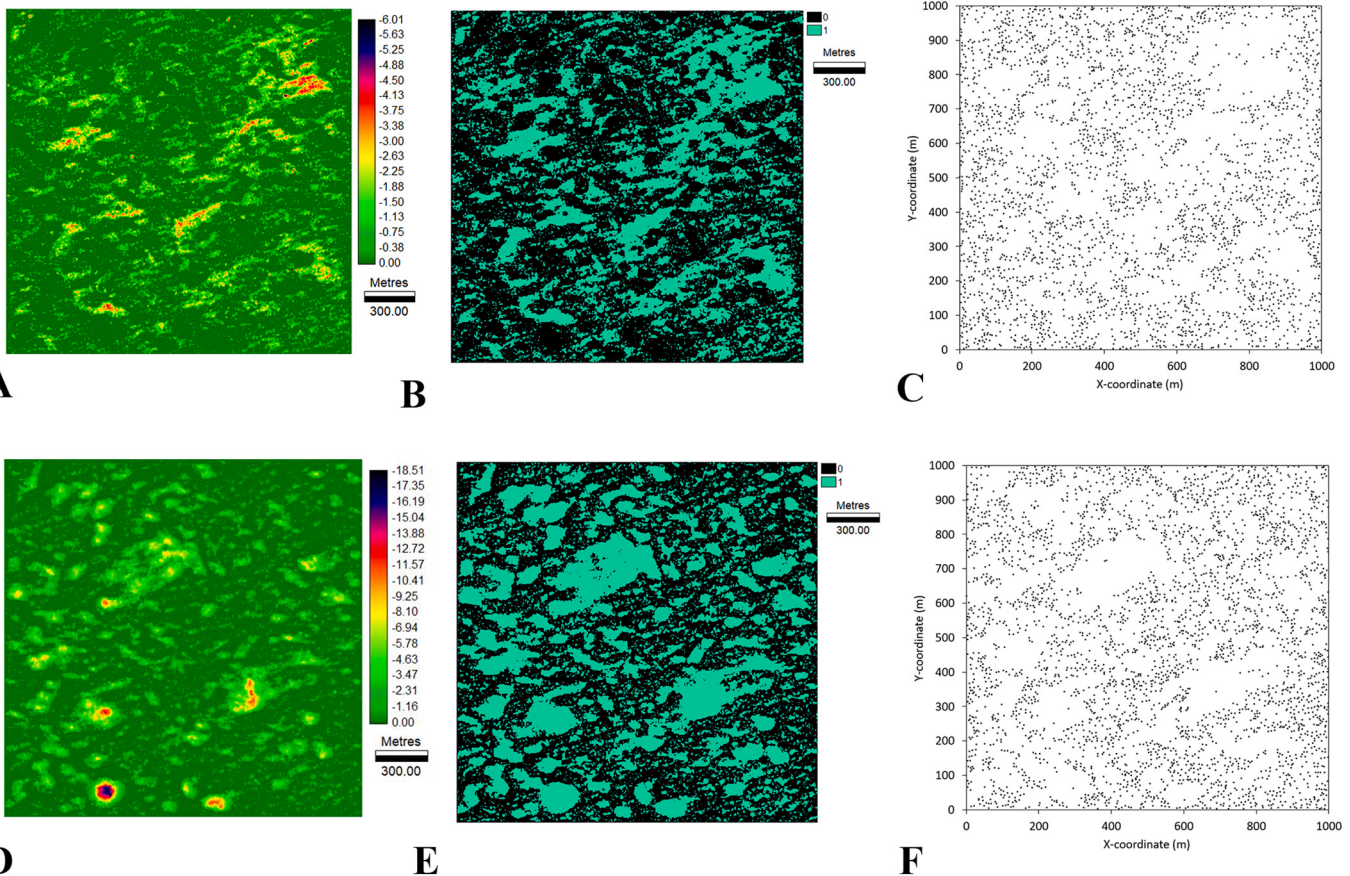


Fig. 8. Volcanic terrain (VT). A. Closed terrain depressions. B. Binary map of closed terrain depressions. C. Point map of the centroids of closed terrain depressions. D. Terrain mounds. E. Binary map of mounds. F. Point map of the centroids of mounds.

depression with respect to the lowest altitude of its rim, which defines the depth of the depression with respect to its potentiometric surface, i.e., the level to which fluid would rise in a depression.

2.3. Identification and delineation of terrain mounds

The method for identifying and mapping mounds is identical to that of identifying depressions, but the pit removal algorithm is applied to the DEM with the sign reversed (i.e., a DEM multiplied by -1) as sketched in Fig. 6. The mounds are obtained as the closed depressions of the sign-reversed DEM. If desired, positive altitudes can be obtained by multiplying the map of mounds by -1 .

2.4. Morphometric analysis of depressions and mounds

The maps of depressions and mounds provide planetary geologists with a means of visually interpreting the images, which can be enhanced with the capabilities of a Geographical Information System in the sense of zooming in and out, reclassifying, using colour saturations, overlaying with other layers of information, etc. In addition, because these maps are raster layers of numerical data (depth of depressions with respect to their rim) they are particularly suitable for numerical morphometric analysis.

Firstly, because depression maps and mound maps are calculated in raster layers with the same specification (number of columns and rows, spatial resolution and geographical coordinates) as the original DEM file, they can be exactly superposed. Thus, altitudes, slopes, orientation and any other terrain variable obtained from the DEM can be assigned to any depression or mound and the correlations between depression depths and altitude, slope and orientation can be calculated. The

statistics of depression depths can be calculated both globally for any test site or locally for particular sub-regions of the test site. The size (area and volume) of each depression can be calculated and morphometric parameters such as circularity, preferential directions or cross-sections, can be calculated. The same morphometric parameters can be estimated for mounds. The size-distributions of depressions and mounds are also of interest in assessing the possible fractal character of those geomorphologies (Reams, 1992; Seckell et al., 2013; Pardo-Igúzquiza et al., 2019). Density maps of depressions and mounds can easily be calculated; exhaustive numerical descriptions of each depression or mound can be generated; and depressions and mounds that meet some criterion, such as having an area greater or less than a given threshold, can be identified. Pardo-Igúzquiza et al. (2016) shows the calculation of many of these parameters for metric spatial-scale closed depressions in a karst area on Earth. The possibilities of morphometric analysis can be extended by transforming the maps of depressions or mounds into point maps by substituting each depression or mound by its centroid. Marked point fields can be obtained by assigning to each point an attribute (the mark) of the depression or mound (e.g., depth, height, area, volume, basal width, crater width, slope of flanks, or their respective ratios.). Furthermore, statistics of the morphometric parameters can be calculated globally or locally, and two thresholds can be applied to select individual depressions or mounds. One of these thresholds is the minimum depth (height) for a pixel to be considered as part of a depression (mound) and the other is an area threshold (or number of pixels) so that only depressions (mounds) larger than a given size are considered. Spatial relationships can be assessed between the maps of depressions and mounds or between their respective point maps. These morphometric parameters can be used to compare different areas of Mars or to compare areas of Mars with Earth analogues.

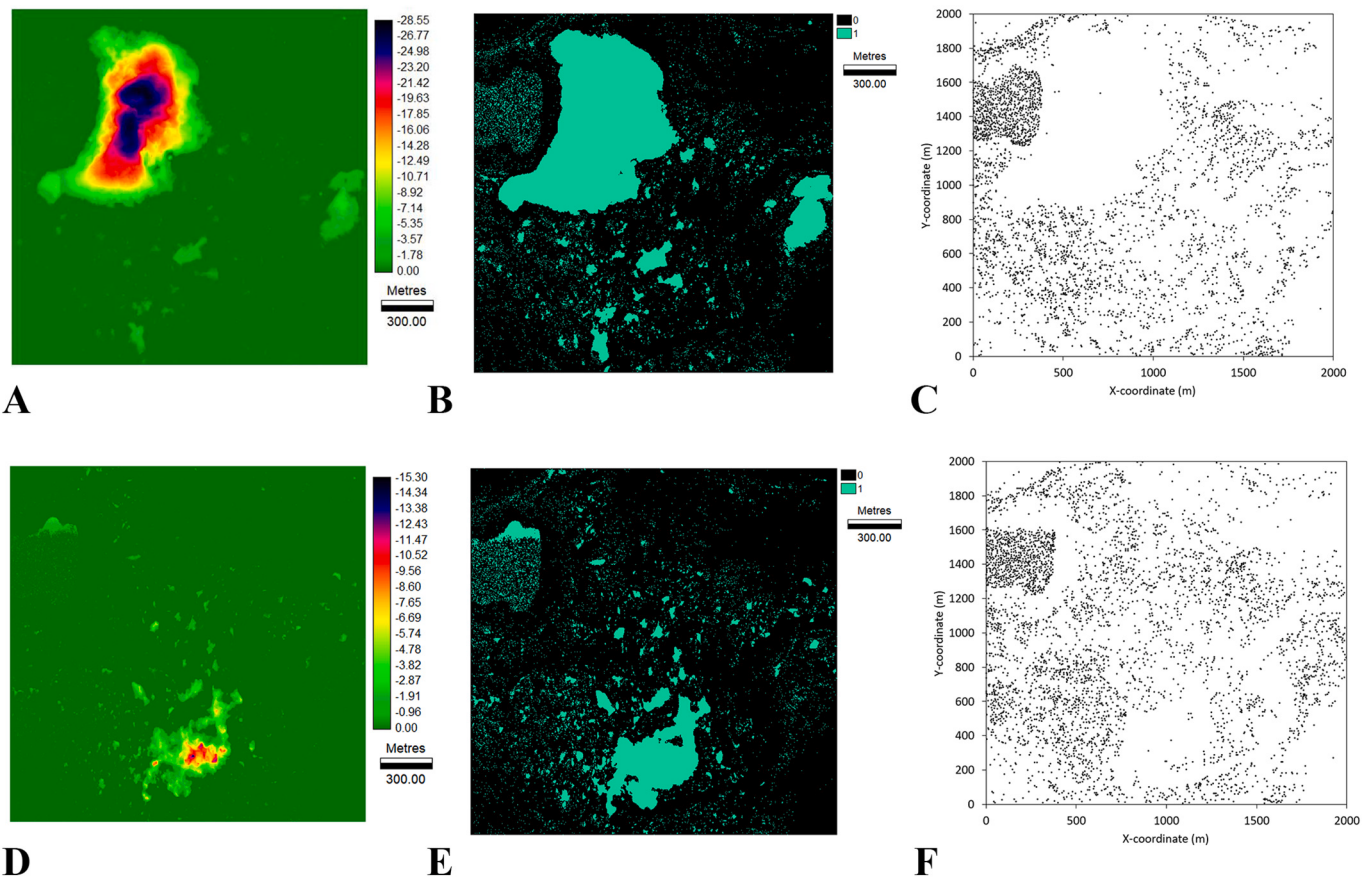


Fig. 9. Hydrated terrain (HT). A. Closed terrain depressions. B. Binary map of closed terrain depressions. C. Point map of the centroids of closed terrain depressions. D. Terrain mounds. E. Binary map of mounds. F. Point map of the centroids of mounds.

Table 2

Statistics of closed terrain depressions and mounds in the pilot areas. Each pilot area is a square of 2 km by 2 km. The statistics for depressions are total number of depressions, density of depressions (number of depressions per hectare), number of one-cell depressions, percentage of one-cell depressions with respect to the total number of depressions and size of the largest depression. The statistics for mounds are the same as the previous ones. All the DEMs have a spatial resolution of 1 m except those marked with an asterisk (*), which have a spatial resolution of 2 m. Thus, one-cell depressions represent depressions with an area of 1 m² or 4 m², for the 1 m and 2 m DEMs respectively.

| Terrain type (test sites) | Depressions (Ds) | | | | | Mounds (Ms) | | | | |
|------------------------------|------------------|--------------------------------------------------|------------------------------|-----------------------------------------------|-----------------------------------------------------------|-----------------|--------------------------------------------------|------------------------------|--------------------------------------|------------------------------------------------------|
| | Number of Ds | Density. Ds inside square 100 m × 100 m | Number of one-pixel Ds | Percentage of one-pixel depressions (%) | Size of the largest depression (m ²) | Number of Ms | Density. Ms inside square 100 m × 100 m | Number of one-pixel Ms | Percentage of one-pixel Ms (%) | Size of the largest mound (m ²) |
| Aeolian | 22,682 | 57 | 4548 | 20.1 | 65,504 | 23,126 | 58 | 4769 | 20.6 | 35,849 |
| Volcanic (*) | 4415 | 11 | 812 | 18.4 | 255,464 | 4812 | 12 | 872 | 18.1 | 159,728 |
| Hydrated | 13,732 | 34 | 3462 | 25.2 | 585,862 | 16,213 | 41 | 4044 | 24.9 | 167,937 |
| Cratered (*) | 4462 | 11 | 688 | 15.4 | 99,652 | 4250 | 11 | 668 | 15.7 | 122,936 |
| Reticulate | 3907 | 10 | 621 | 15.9 | 79,938 | 3025 | 8 | 325 | 10.7 | 76,023 |
| Sublimated | 118,441 | 296 | 44,976 | 38.0 | 2796 | 110,744 | 278 | 39,985 | 36.1 | 3,05 |

3. Results

The methodologies for mapping closed depressions and mounds were applied to the six test sites described above. The graphical results are shown in Figs. 7A-F to 12A-F for aeolian, volcanic, hydrated, cratered, reticulate and sublimated terrains respectively. For all cases, the maps in Figs. 7A to 12A show the depth (negative value) of each depression from its rim. The maximum depths are -5.95, -6.01, -28.55, -10.92, -2.80 and -5.39 m for the six test sites respectively (Table 1). The maximum depth of -28.55 m corresponds to the hydrated terrain of the DEM that has the highest relief amplitude (difference between maximum and minimum altitudes) of 185 m (Table 1 and

Fig. 4). Remarkably, the cratered terrain with the smallest relief amplitude of 20 m has a maximum depth of -10.92 m which is half the relief amplitude. The binary maps in Figs. 7B to 12B have a value of 1 (green) for the area occupied by depressions and a value of 0 (black) for the areas with no depressions. The percentage of the surface of each test site occupied by depressions is given in Table 1 and ranges from 18% in the aeolian terrain (Fig. 7B) to 34% in the volcanic terrain (Fig. 8B). The maps in Figs. 7C to 12C show the fields of points obtained from the depression maps by representing each depression in the depression maps of Figs. 7A to 12A, as a point defined by the centroid. The map of depressions (and mounds) is a raster map and each depression (or mound) is defined by a set of connected pixels with depth (or altitude) for

Table 3

Statistics of closed terrain depressions and mounds in the pilot areas. Each pilot area is a square of 2 km by 2 km. The statistics for depressions are the total number of depressions (N) with area greater than, or equal to, 4 m^2 , and the statistics of the area of depressions: minimum, mean, 25 percentile, median (i.e. 50 percentile) and 90 percentile. The maximum, i.e. the area of the largest depression is given in the last column of Table 1. The same statistics have been estimated for mounds. All the DEMs have a spatial resolution of 1 m except those marked with an asterisk (*), which have a spatial resolution of 2 m. Min. is minimum and perc. is percentile.

| Terrain type (test sites) | Depressions | | | | | | Mounds | | | | | |
|---------------------------|-------------|-----------------------|-----------------------|---------------------------|-------------------------|---------------------------|--------|-----------------------|-----------------------|---------------------------|-------------------------|---------------------------|
| | N | Min. (m^2) | Mean (m^2) | 25 perc. (m^2) | Median (m^2) | 90 perc. (m^2) | N | Min. (m^2) | Mean (m^2) | 25 perc. (m^2) | Median (m^2) | 90 perc. (m^2) |
| Aeolian | 12,734 | 4.0 | 55.2 | 6.0 | 10.0 | 40.0 | 13,389 | 4.0 | 41.3 | 6.0 | 10.0 | 38.0 |
| Volcanic (*) | 4415 | 4.0 | 311.9 | 8.0 | 24.0 | 232.0 | 4812 | 4.0 | 356.0 | 8.0 | 24.0 | 228.0 |
| Hydrated | 6833 | 4.0 | 127.9 | 5.0 | 9.0 | 38.0 | 8135 | 4.0 | 51.9 | 5.0 | 9.0 | 43.0 |
| Cratered (*) | 4462 | 4.0 | 227.4 | 8.0 | 24.0 | 160.0 | 4250 | 4.0 | 161.2 | 8.0 | 24.0 | 184.0 |
| Reticulate | 2618 | 4.0 | 366.5 | 8.0 | 19.0 | 342.5 | 2322 | 4.0 | 625.4 | 12.0 | 41.0 | 876.5 |
| Sublimated | 42,497 | 4.0 | 23.3 | 5.0 | 9.0 | 46.0 | 42,835 | 4.0 | 22.8 | 5.0 | 10.0 | 44.0 |

Table 4

Statistics of the depth (relative to the rim of the depression) of closed terrain depressions and statistics of altitude of mounds (relative to the rim of the mound) in the pilot areas for the number of depressions (N) with area greater than, or equal to, 4 m^2 . The statistics are mean depth and maximum depth. All the DEMs have a spatial resolution of 1 m except those marked with an asterisk (*), which have a spatial resolution of 2 m.

| Terrain type (test sites) | Depressions | | | Mounds | | |
|---------------------------|-------------|----------------|-------------------|--------|---------------|------------------|
| | N | Mean depth (m) | Maximum depth (m) | N | Mean high (m) | Maximum high (m) |
| Aeolian | 12,734 | -0.95 | -5.95 | 13,389 | 1.07 | 11.01 |
| Volcanic (*) | 4415 | -0.97 | -6.00 | 4812 | 1.84 | 18.50 |
| Hydrated | 6833 | -8.28 | -28.55 | 8135 | 1.53 | 15.29 |
| Cratered (*) | 4462 | -0.74 | -10.92 | 4250 | 0.24 | 1.70 |
| Reticulate | 2618 | -0.50 | -2.80 | 2322 | 0.92 | 7.73 |
| Sublimated | 42,497 | -0.31 | -5.39 | 42,835 | 0.25 | 4.45 |

mounds) larger than zero. Thus, the centroid of the i^{th} depression (X_i^c, Y_i^c) is calculated as a weighted average of the coordinates of each of the cells that form the depression weighted by the depth of each cell:

$$X_i^c = \frac{1}{\sum_{k=1}^{n_i} Z_i} \sum_{j=1}^{n_i} X_i Z_i$$

$$Y_i^c = \frac{1}{\sum_{k=1}^{n_i} Z_i} \sum_{j=1}^{n_i} Y_i Z_i$$

where each cell that forms part of a single depression has coordinates (X_i, Y_i) of the centre of the cell together with the depth (Z_i) of the cell. Another representative point could be the point of deepest depth of each depression.

The maps in Figs. 7D to 12D show the altitudes of the mounds with respect to their rims. They have a negative value because of the calculation method (Fig. 6) but the negative sign can be ignored in the interpretation or could be multiplied by minus one to yield positive values. The maximum altitudes (Table 1) are 11.02, 18.51, 15.30, 1.70, 7.73 and 4.46 m for the six test sites respectively. The maximum of 18.51 m corresponds to a volcanic cone clearly seen in the bottom left of Fig. 8D. The smallest mound of 1.70 m in the cratered terrain corresponds to a small mound formed by ejected impact material as seen in Fig. 10D. The maps in Figs. 7E to 12E are binary with a value of 1 (green) for areas occupied by mounds and a value of 0 (black) for areas with no depressions. The percentage of the surface of each test site that is occupied by mounds is given in Table 1 and ranges from 11% in the hydrated terrain (Fig. 9D) to 43% in the volcanic terrain (Fig. 8B). The volcanic and reticulate terrains have higher percentages of their surfaces occupied by mounds than by depressions and the opposite applies to the aeolian, hydrated and cratered terrains. The sublimated terrain is

perfectly compensated terrain in which the percentage of mounds is the same as the percentage of depressions, which is readily explained by the process that generates this type of landscape as discussed below. The maps in Figs. 7F to 12F show the point fields obtained from the mound maps by representing each mound as a point.

The highest number of 118,441 depressions (Table 2) is in the sublimated terrain (Fig. 12) and the lowest number is 3907 depressions in the reticulate terrain (Fig. 11). This implies a difference in the density of depressions (number of depressions per hectare, i.e., a square of 100 m \times 100 m) of 296 and 10 for the sublimated and reticulate terrains respectively. The fifth column of Table 2 lists the percentages of one-cell depressions (depressions of around 1 m^2 for the 1 m resolution DEMs or 4 m^2 for the 2 m resolution DEMs, marked with an asterisk in the Table), which varies from 38% for the sublimated terrain to 15.4% for the cratered terrain. The highest number of mounds is 110,744 (Table 2) in the sublimated terrain (Fig. 12) and the lowest number is 3025 in the reticulate terrain (Fig. 11). This implies a difference in the density of mounds (number of mounds per hectare) of 278 and 8 for the sublimated and reticulate terrains respectively. The fifth column of Table 2 lists the percentages of one-cell mounds (mounds of around 1 m^2 for the 1 m resolution DEMs or 4 m^2 for the 2 m resolution DEMs, marked with an asterisk in the Table), which varies from 36.1% for the sublimated terrain to 10.7% for the reticulate terrain. Thus, the maximum and minimum numbers of depressions and mounds in the sublimated and reticulate terrains are comparable given their similar numbers and densities.

Because there are two spatial resolutions for the DEMs of 1 m for aeolian, hydrated, reticulate and sublimated terrains and of 2 m for volcanic and cratered terrains, the statistics of depressions and mounds have also been calculated for depressions and mounds with areas greater than or equal to 4 m^2 . The results are shown in Table 3 for depressions and mounds. In Table 3 the highest number of depressions is 42,497 for the sublimated terrain and the lowest is 2618 for the reticulate terrain. The maximum mean size of depressions is 366.5 m^2 for the reticulate terrain but the maximum median is 24 m^2 for the volcanic and cratered terrains. The highest number of mounds (Table 3) is 42,835 for the sublimated terrain and the minimum is 2322 for the reticulate terrain. The maximum mean size of mounds is 625.4 m^2 for the reticulate terrain and the maximum median is 41 m^2 also for the reticulate terrain. For depressions with an area greater than or equal to 4 m^2 , Table 4 shows the maximum mean depth of the depressions is -8.28 m for the hydrated terrain and for all other terrains the mean depth is less than -1 m . For mounds with an area greater than or equal to 4 m^2 , Table 4 shows the maximum mean altitude of the mounds is 1.84 m for the volcanic terrain, followed by 1.53 m for the hydrated terrain. The mean altitude of the mounds for the sublimated terrain is 0.25 m .

The mean shape of the closed depressions can be characterized by their main elongation trends, that is, the directions along which the depression has a elongation trend giving an irregular depression differing significantly from a regular circular form. Circular depressions do not have any elongation trend but they developed in all directions.

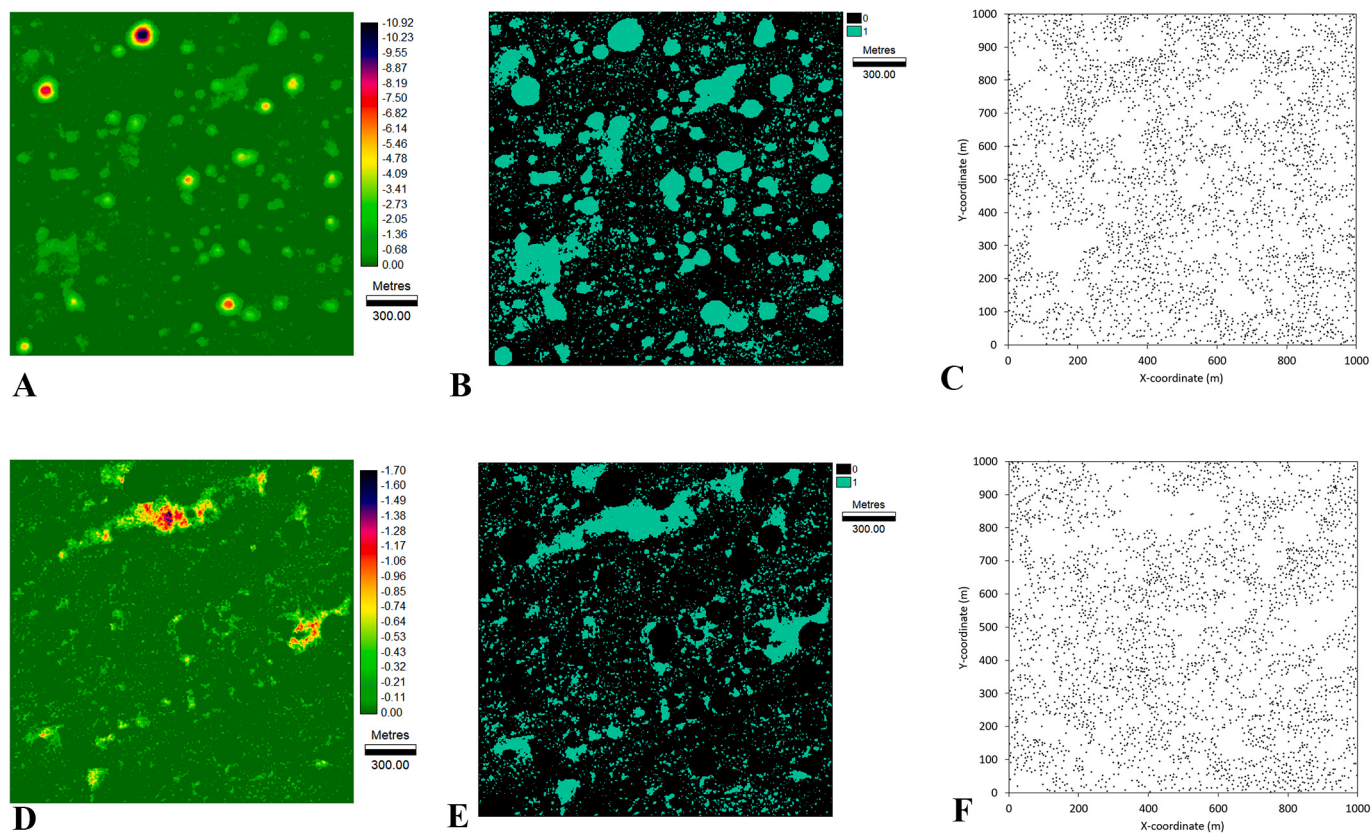


Fig. 10. Cratered terrain (CT). A. Closed terrain depressions. B. Binary map of closed terrain depressions. C. Point map of the centroids of closed terrain depressions. D. Terrain mounds. E. Binary map of mounds. F. Point map of the centroids of mounds.

The elongation trends were calculated for each depression and are represented in the rose diagram (Richardson et al., 2021; Mazzarini and Isola, 2021) in Fig. 13A. If most of the depressions in a given type of terrain were circular, the rose diagram would be a circle, thus not indicating any preferential direction of development. However, as can be seen in Fig. 13A, the rose diagrams for all terrains are more or less elliptical with main directions of development approximately N-S, E-W, N-S, N-S, NE-SW and NW-SE for the aeolian, volcanic, hydrated, cratered, reticulate and sublimated terrains respectively. The rose diagrams for the mounds are shown in Fig. 13B, in which the main directions of development are approximately N-S, E-W, N-S, N-S, NE-SW and NW-SE for the aeolian, volcanic, hydrated, cratered, reticulate and sublimated terrains respectively. Thus, for each terrain type, the main directions of development for the mounds are the same as those for the depressions but the shapes of the mound ellipses are generally more elongated, particularly for RT, HT and ST, implying a stronger directionality in the mounds in this terrain. The rose diagrams of the point-fields (centroids of depressions and mounds) are shown in Fig. 14A and B respectively. The rose diagrams of the directions between points were calculated using the directions of the $N(N-1)/2$ segments that join each point with all others (Mazzarini and D'Orazio, 2003; Bleacher et al., 2009; Lezama et al., 2015). These diagrams show that only the hydrated and reticulate terrains show any preferential lineament of points and these are in the NW-SE and NE-SW directions respectively. Further morphometric analysis, such as nearest-neighbour classification (Balogh et al., 2007; Bleacher et al., 2009; Le Corvec et al., 2013), could be applied to the point fields of the depressions and mounds or to the merger of both fields.

The histograms of the areas of the depressions are shown in Fig. 15. These histograms indicate two distinct behaviours with the aeolian, hydrated and sublimated terrains forming one group and the volcanic and cratered terrains forming a second group; the reticulate terrain is

intermediate between these two groups. The same groups can be seen for the histograms of the areas of the mounds in Fig. 16.

The log-log plots in Figs. 17 and 18 show the fractal character of the size-distributions of the metric spatial-scale closed depressions and mounds. The fractal character of the spatial distribution of a field of points representing mounds has been demonstrated by others (Pozzobon et al., 2019; De Toffoli et al., 2018, 2019). Fig. 17 shows that the aeolian, sublimated and hydrated terrains form a group in which the slopes of the log-log plots are higher (thus a higher value of a power law exponent) than those of the group comprising the volcanic, cratered and reticulate terrains. A similar analysis applies to the plots of the mounds shown in Fig. 18. The implications of these results are discussed below.

Many other morphometric analyses could be undertaken on the depressions and mounds obtained by the methodology proposed in this work. For example, the joint analysis of the point fields of depressions and mounds would be of particular interest, but it is not pursued here.

4. Discussion

The joint analysis of the six terrain types shows that the aeolian, hydrated and sublimated terrains exhibit similar fractal behaviour, which may be the result of a detached geomorphology, that is, geomorphic processes on detached material such as sand in the case of aeolian terrain (sand dunes) and dry ice in the case of sublimated terrain. There is also a bedrock geomorphic process in the volcanic, cratered and reticulate terrains. The hydrated terrain appears not to be the result of detached geomorphology perhaps because of the plastic behaviour of outcropping rocks interpreted as evaporates.

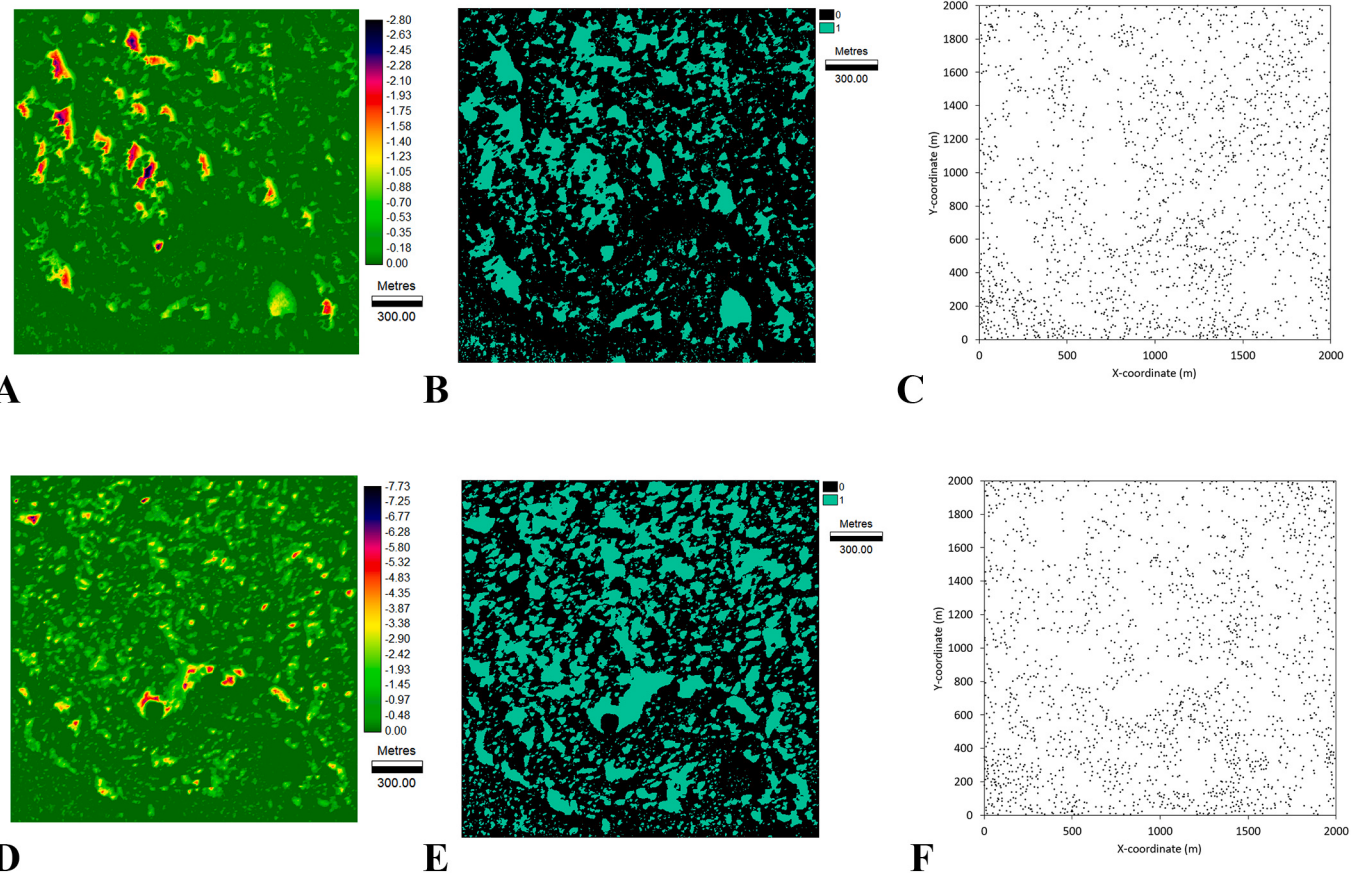


Fig. 11. Reticulate terrain (RT). A. Closed terrain depressions. B. Binary map of closed terrain depressions. C. Point map of the centroids of closed terrain depressions. D. Terrain mounds. E. Binary map of mounds. F. Point map of the centroids of mounds.

4.1. Aeolian landscape in Melas Chasma: blowouts and pan marginal lunette dunes

The map of closed depressions of the aeolian landscape test site in Fig. 7A shows that they are not complex depressions, but simple elliptical depressions elongated in the NW-SE direction. In Melas Chasma, surficial units are interpreted as the product of aeolian and mass-wasting processes. The absence of impact craters in most surficial units suggests that these are the product of relatively young and potentially still active processes (Edgar et al., 2019). These depressions could be saucer blowout morphologies (Barchyn and Hugenholtz, 2013), that is, deflation basins, in which the sand has been removed by the wind. It is clear from the map of mounds in Fig. 7F that the mounds are consistent with a dune field. In particular, given their association with the depressions, they may be pan margin lunette dunes (Lawson and Thomas, 2002) and their morphometric parameters may be of interest (Liu et al., 2018). Furthermore, the dunes in Fig. 7D appear to be isolated and, as shown in Fig. 19A, the depressions are not intra-dune, i.e., the depressions have not been formed by the dunes acting as barriers but by wind deflation. Dune patterns are relevant in understanding aeolian sediment flux, sediment sources and wind directions (Chojnacki et al., 2010). In addition, these maps provide a means of studying the aeolian processes and dune morphology, slip-faces and the topographic influences on prevailing wind directions (Hobbs et al., 2010). Numerical wind flow modelling using these blowouts (Smyth et al., 2019) could also be used to explore wind dynamics on the Martian landscape.

4.2. Volcanic landscape in the northern part of Ulysses Tholus: erosion-transformed depressions and mounds

Fig. 8A is a map of the closed depressions of the volcanic landscape test site. These depressions have complex shapes with a preferential E-W orientation (Fig. 12, VT) and a mean size of 311.0 m² (Table 3). Karátsón et al. (1999) provide a review of erosion-modified, erosion-transformed and erosion-induced depressions in volcanic terrains on Earth. In Fig. 8A only small summit volcano depressions and a clear flank volcano depression can be identified in the bottom left, which is related to a small volcano cone clearly identified in the mounds map in Fig. 8D. The complex depressions in Fig. 8A may be the results of lava flows or products of explosive volcanism (Hynek et al., 2003; Brož et al., 2014). Explosive volcanism has been postulated in relation to the larger, kilometric-size volcanic cones (Brož and Hauber, 2012) located a few kilometres north of the test site as can be seen in the HiRISE image (Fig. 2, VT) and which could have been modified by mass-wasting, land sliding and other erosion processes. Thus, the depressions shown in Fig. 8A could be classified as erosion-transformed volcanic depressions. Fig. 19B shows the strong intricacy between closed depressions and mounds of the Martian volcanic terrain. Volcanic processes can also induce terrain depressions if there is underground ice (Levy et al., 2017). The morphometry of larger volcanic cones in a much larger area, can be found in Brož et al. (2015). Among the mounds mapped in Fig. 8D, there is only one very obvious volcanic cone, which is shown in detail in Fig. 20B (VT).

4.3. Hydrated landscape inside Ius Chasma: an evaporite karst

The map of closed depressions in the hydrated landscape test site is

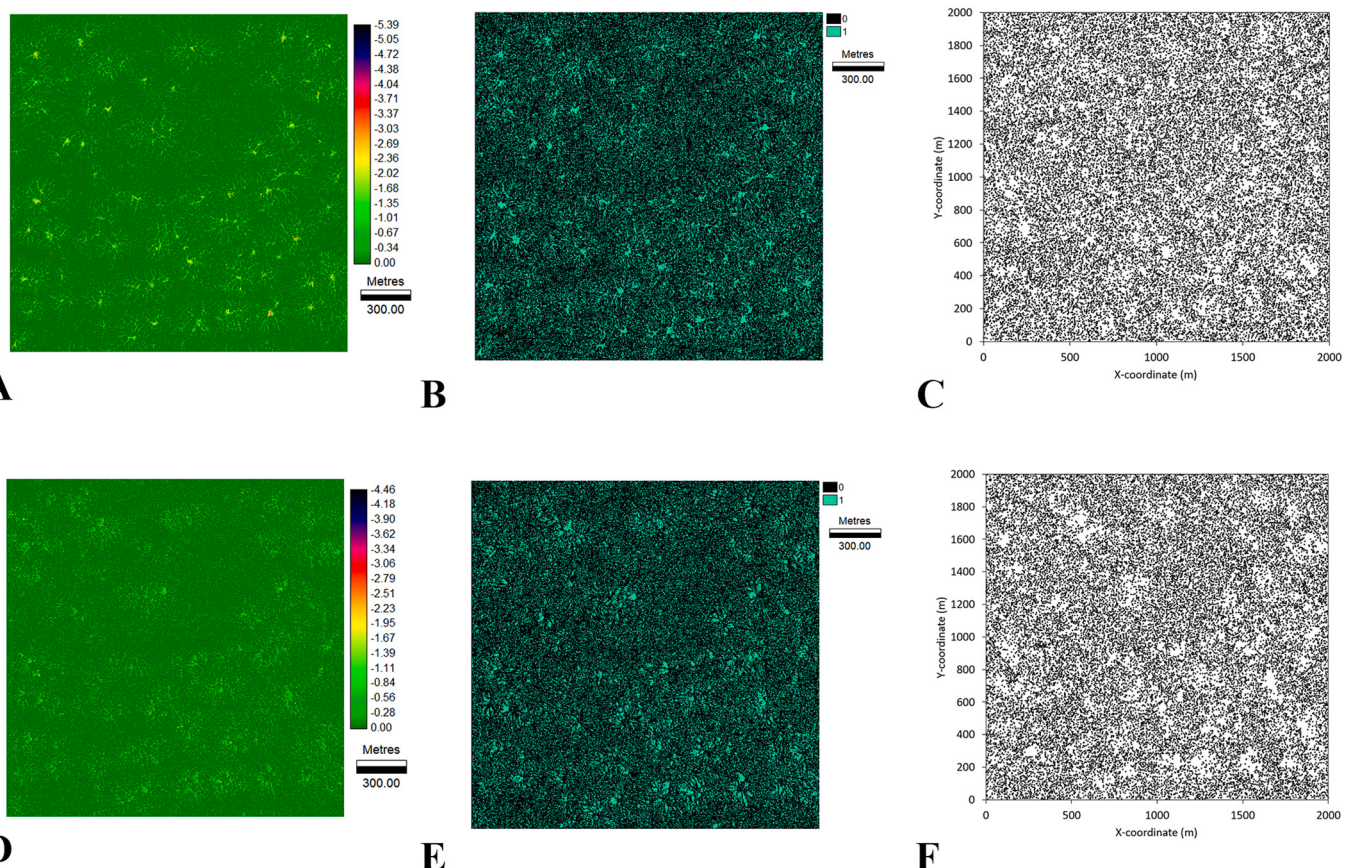


Fig. 12. Sublimated terrain (ST). A. Closed terrain depressions. B. Binary map of closed terrain depressions. C. Point map of the centroids of closed terrain depressions. D. Terrain mounds. E. Binary map of mounds. F. Point map of the centroids of mounds.

shown in Fig. 9A. Despite the dominance of a large, irregular and complex depression with a surface area of 585,862 m², representing around 14% of the surface of the study area, the total number of depressions is 13,732 which is greater than the number of depressions in all other types of landscapes (see Table 2). The binary map in Fig. 9B shows the swirling geometry of sedimentary layering similar to that of salt and gypsum diapirs on Earth (Bosák et al., 1999; Hudec and Jackson, 2007) and similar to the diapirism found in the Hellas basin floor (Bernhardt et al., 2016). Hydrated sulphates have been identified on similar light-toned layered terrains on Mars by using spectral signatures (Gendrin et al., 2005). The mounds in Fig. 9D also display complex shapes that are possibly the result of plastic behaviour of the outcropping rocks in this terrain.

4.4. Cratered landscape in the northern flank of Tharsis Tholus volcano: the typical crater landscape

The map of closed depressions of the cratered landscape test site is shown in Fig. 10A. This is a landscape that would be the expected result of impact cratering at the metric scale. It is a pitted landscape dominated by impact craters and where the only mounds are small ones in the material ejected by the impact; see Fig. 10D and the detail shown in Fig. 20B (CT). This landscape has not had any significant resurfacing in recent times and, if the conservation of impact craters is used as a proxy of relative age, it may possibly be the oldest of the analysed landscapes.

A total of 4462 closed depressions have been mapped and their mean size is 227.4 m². The N-S direction of the shape of the depressions shown in the rose diagram CT in Fig. 12 may be due to the pre-existing volcanic topography that has been modified by the impact craters and the ejected material. In addition, if there was ice close to the surface, the heat of the impact would have induced its sublimation and increased the size of the depressions (Dundas et al., 2015; Viola et al., 2015; Levy et al., 2017).

4.5. Reticulate landscape in Lycus Sulci: a jigsaw puzzle pattern of depressions and mounds

The map of closed depressions of the reticulate landscape test site is shown in Fig. 11A. The binary depressions map in Fig. 11B resembles a jigsaw puzzle. The total surface area occupied by the depressions is 24% which is similar to those of the hydrated, cratered and sublimated terrains. The number of depressions greater than or equal to 4 m² is 2618 which is the lowest of the six types of landscapes. The reticulate terrain has a mean depression size of 366.5 m², which is the largest of the six landscapes. This patterned terrain is similar to, but not quite the same as, fretted terrain (Carr, 2001), brain coral texture terrain (Noe Dobrea et al., 2007) or honeycomb terrain (Bernhardt et al., 2016). We propose the jigsaw puzzle pattern designation for this type of terrain. A possible origin of this pattern could be the downslope movement of wall material caused by viscous deformation of ground ice (Bridges et al., 2010). In addition, the elliptical shapes in the mounds map in Fig. 11D and in the

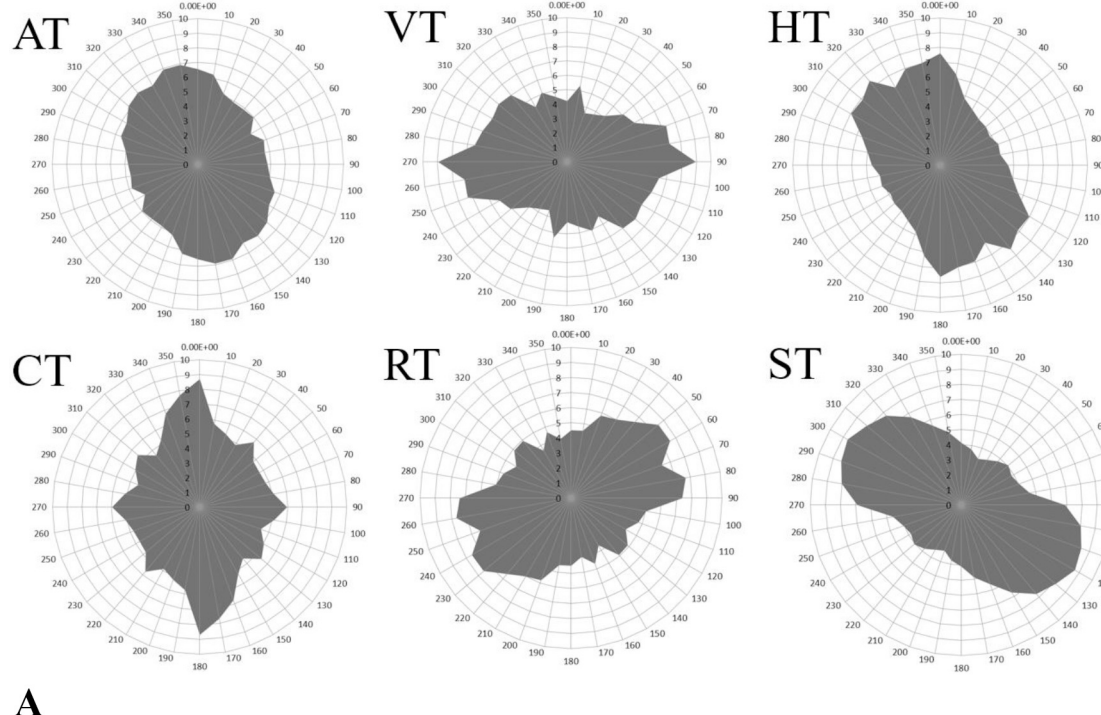
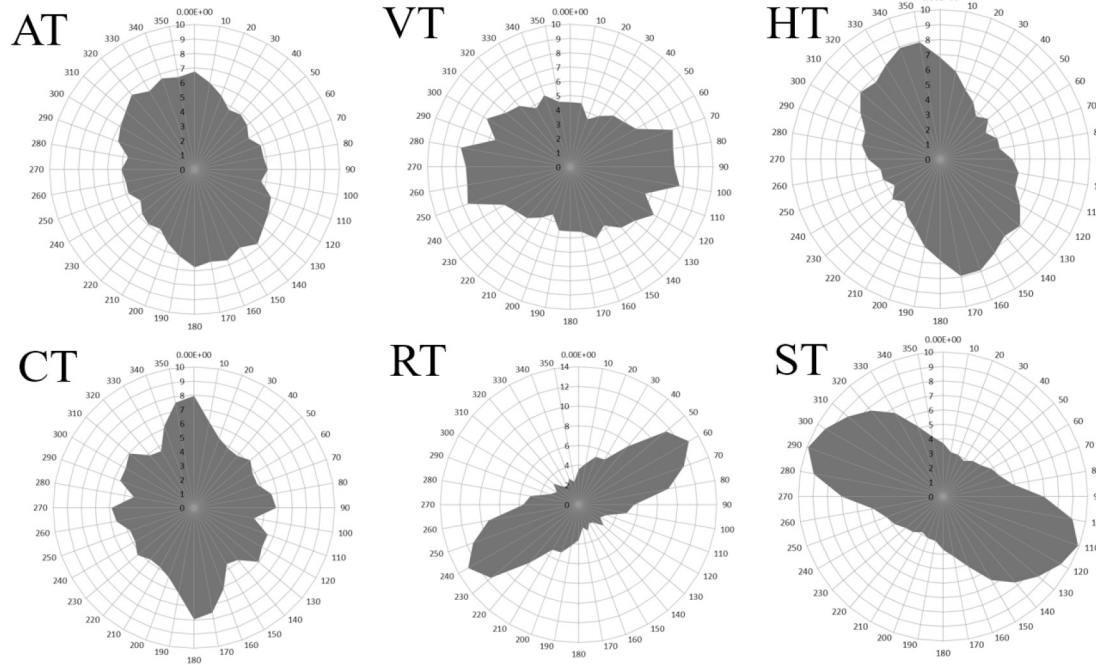
**A****B**

Fig. 13. A. Rose diagram of the directions of the shape of the depressions in aeolian terrain (AT), volcanic terrain (VT), hydrated terrain (HT), cratered terrain (CT), reticulate terrain (RT) and sublimated terrain (ST). B. Rose of directions of the shape of the mounds in aeolian terrain (AT), volcanic terrain (VT), hydrated terrain (HT), cratered terrain (CT), reticulate terrain (RT) and sublimated terrain (ST). (For interpretation of the references to colour in this figure legend, the reader is referred to the web version of this article.)

detailed image in Fig. 20B (RT) indicate that the action of the wind may have contributed to terrain formation (Bridges et al., 2007). Thus, the origin seems to be polygenic and it is very likely that there are strong lithological and structural controls in the formation of the jigsaw puzzle pattern of closed depressions and mounds.

4.6. Sublimated landscape at the Southern pole: negative and positive araneiforms

Fig. 12A is a map of the closed depressions of the sublimated landscape test site. As shown in Fig. 4 (ST) and in the detailed map in

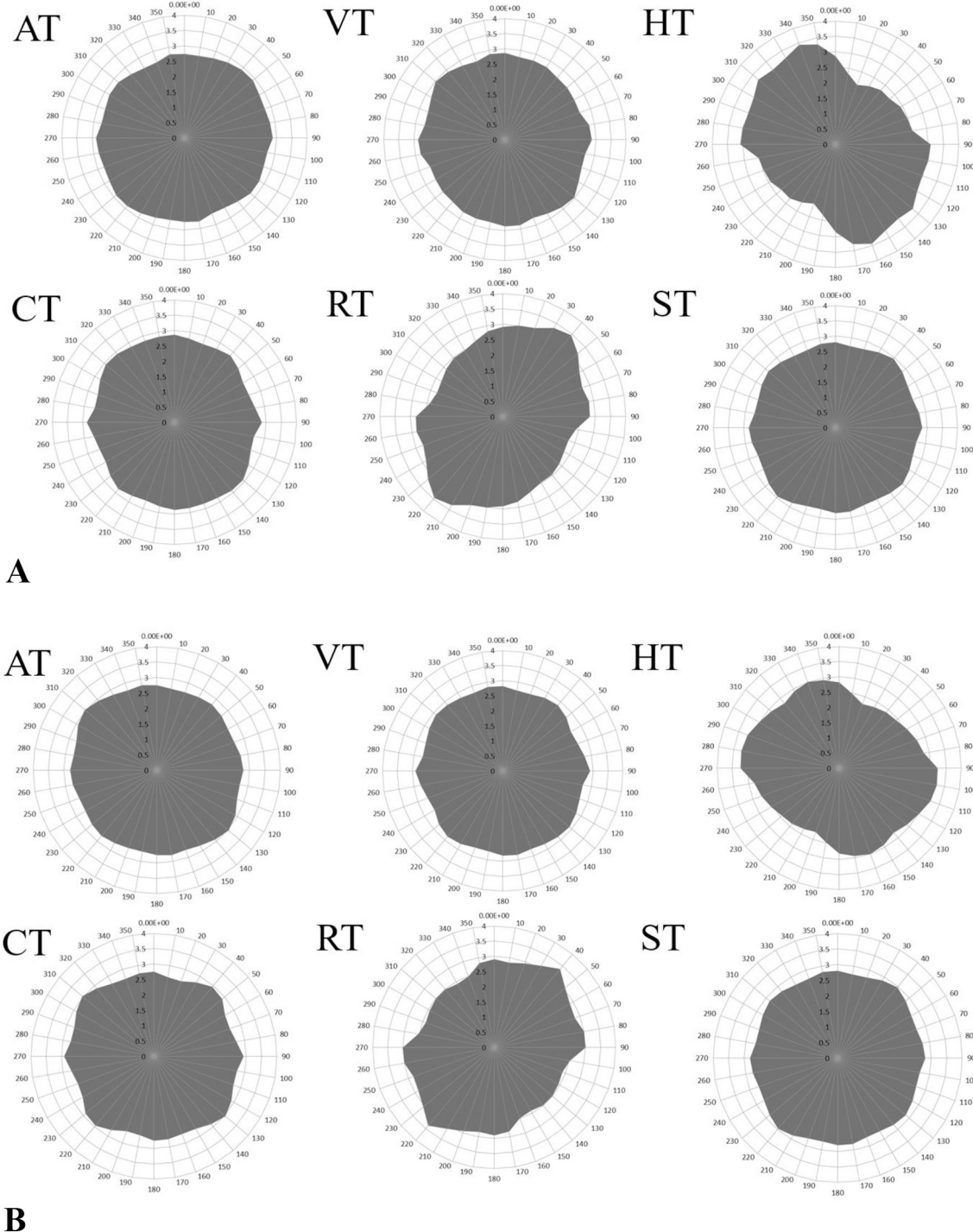


Fig. 14. A. Rose diagram of the directions of the centroids of the depressions in aeolian terrain (AT), volcanic terrain (VT), hydrated terrain (HT), cratered terrain (CT), reticulate terrain (RT) and sublimated terrain (ST). B. Rose diagram of the directions of the centroids of the mounds in aeolian terrain (AT), volcanic terrain (VT), hydrated terrain (HT), cratered terrain (CT), reticulate terrain (RT) and sublimated terrain (ST). (For interpretation of the references to colour in this figure legend, the reader is referred to the web version of this article.)

Fig. 20A (ST), this area has a dendritic network of depressions known as araneiform geomorphology (Kieffer, 2000; Hao et al., 2019) or, more colloquially, as spiders or spider-like patterns (Piqueux et al., 2003). This geomorphology is formed by the seasonal sublimation of CO₂ (Wood and Paige, 1992; de Villiers et al., 2012; Schwamb et al., 2018) and in **Fig. 12A** the legs of the spiders are the depressions that form the

channels carved by the venting of CO₂ gas. These depressions are small with an average area of 23.3 m² (**Table 3**) and are elongated in the NW-SE (**Fig. 13A**) direction which is the general slope of topography in the area (**Fig. 2**, ST). The high density of depressions and mounds per hectare, 296 and 278 respectively, implies a rough terrain with depressions up to 5 m deep and mounds up to 5 m high (**Table 1**). The

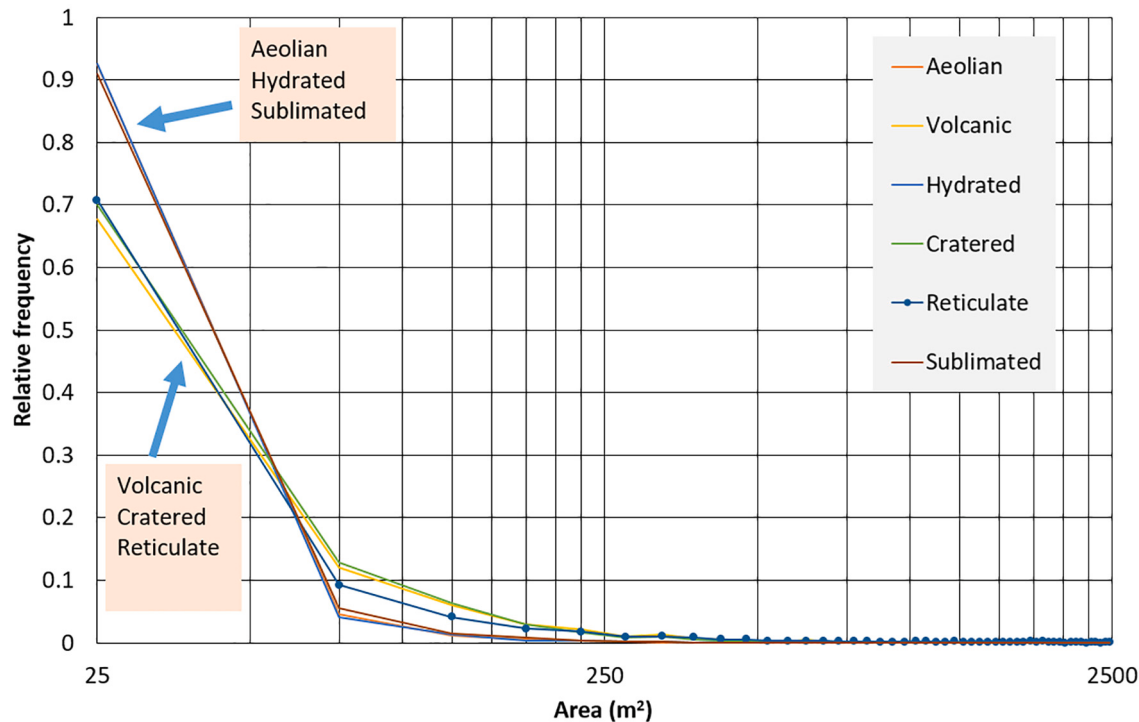


Fig. 15. Histograms of the areas of closed terrain depressions. Two types of distributions of the area of small depressions are clearly visible and are highlighted in the figure. Reticulate is an intermediate case between both groups.

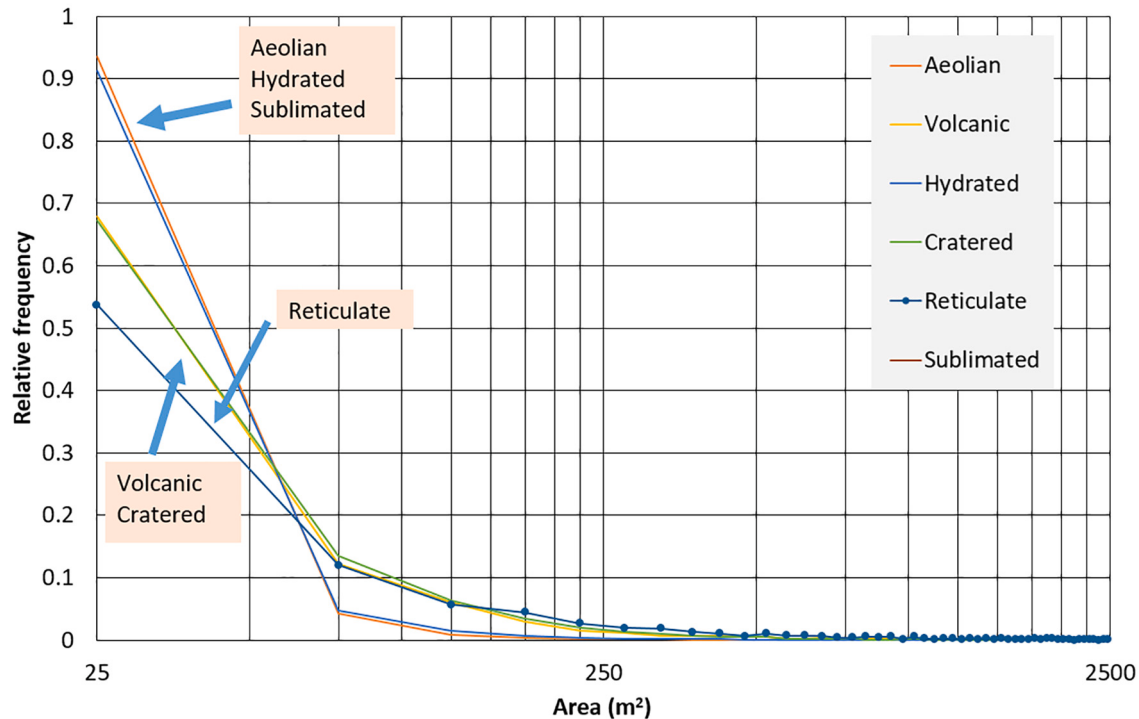


Fig. 16. Histograms of the areas of terrain mounds. Two types of distributions of the areas of small depressions are clearly visible and are highlighted in the figure. Reticulate has a different behaviour to the two main groups and for very small mounds.

mounds shown in detail in Fig. 20B (ST) are located between the channels (i.e., the depressions) and comprise a mixture of granular material and ice. The mounds have the same main NW-SE orientation as the depressions. This terrain is compensated in the sense that it has the same percentage of closed depressions and mounds (Table 2).

A final matter, common to all terrain types, is the issue of 1-pixel depressions i.e., depressions of 1-pixel size or one pixel that is surrounded by pixels of higher altitude. Are the 1-pixel depressions real terrain depressions or are they artefacts in stereo matching algorithms and interpolators? HiRISE DEMs are generated from two images of the

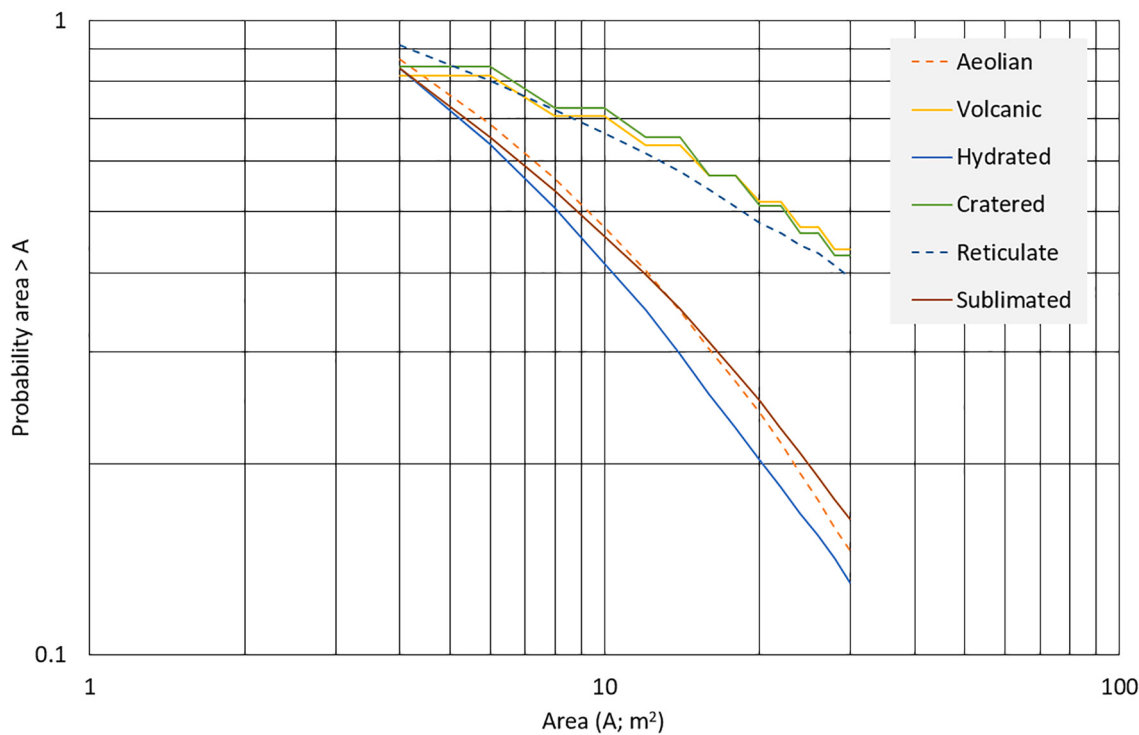


Fig. 17. Log-log plot of area versus probability of a depression chosen at random to be larger than that area. There are two main groups. The first is the larger fractal dimension (slope of the lines) group comprising the aeolian, sublimated, and hydrated. The second is the smaller fractal dimension group comprising the volcanic, cratered and reticulate.

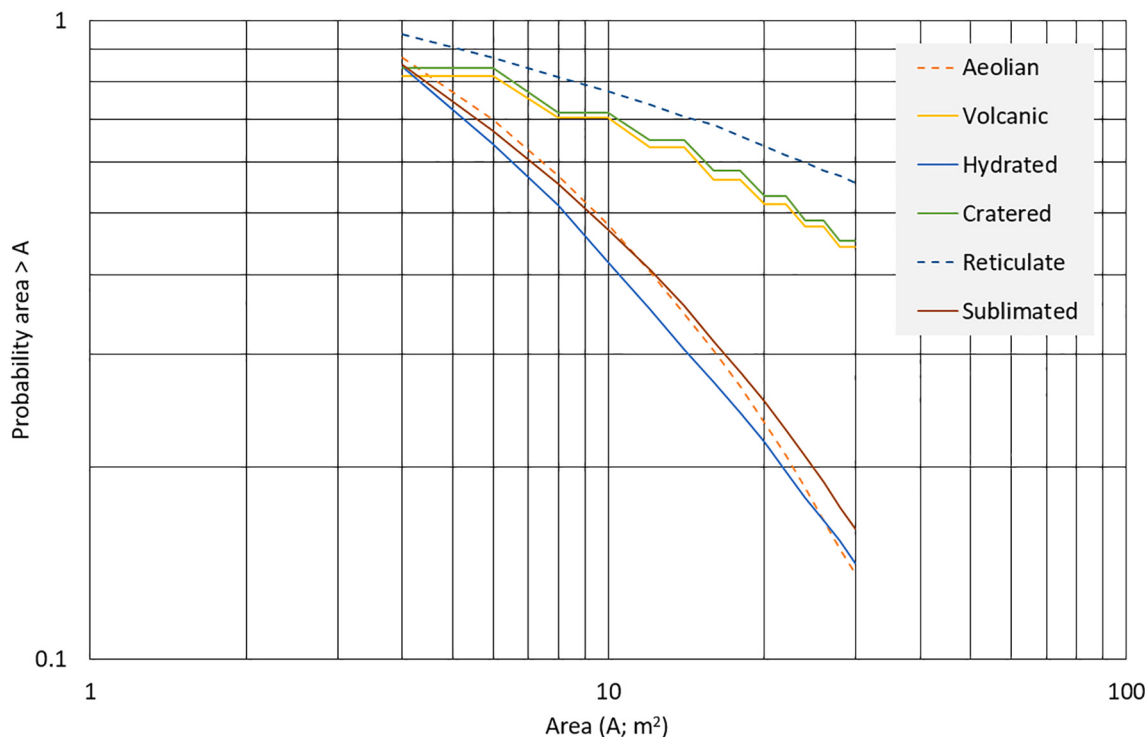


Fig. 18. Log-log plot of area versus probability of a mound taken at random to be larger than that area. There are two main groups. The first is the larger fractal dimension (slope of the lines) group comprising the aeolian, sublimated, and hydrated. The second is the smaller fractal dimension group comprising the volcanic, cratered and reticulate.

same ground area taken from different perspectives. HiRISE images are usually 0.25 m - 0.50 m/pixel, so the post spacing is 1 m – 2 m with a vertical precision in the tens of centimetres (www.uahirise.org/dtm/about.php and Hepburn et al., 2019).

Thus, the planimetric uncertainty is less than 1 m and 1 m wide depressions can be considered real. The altimetric uncertainty is not so important as the spatial errors will be

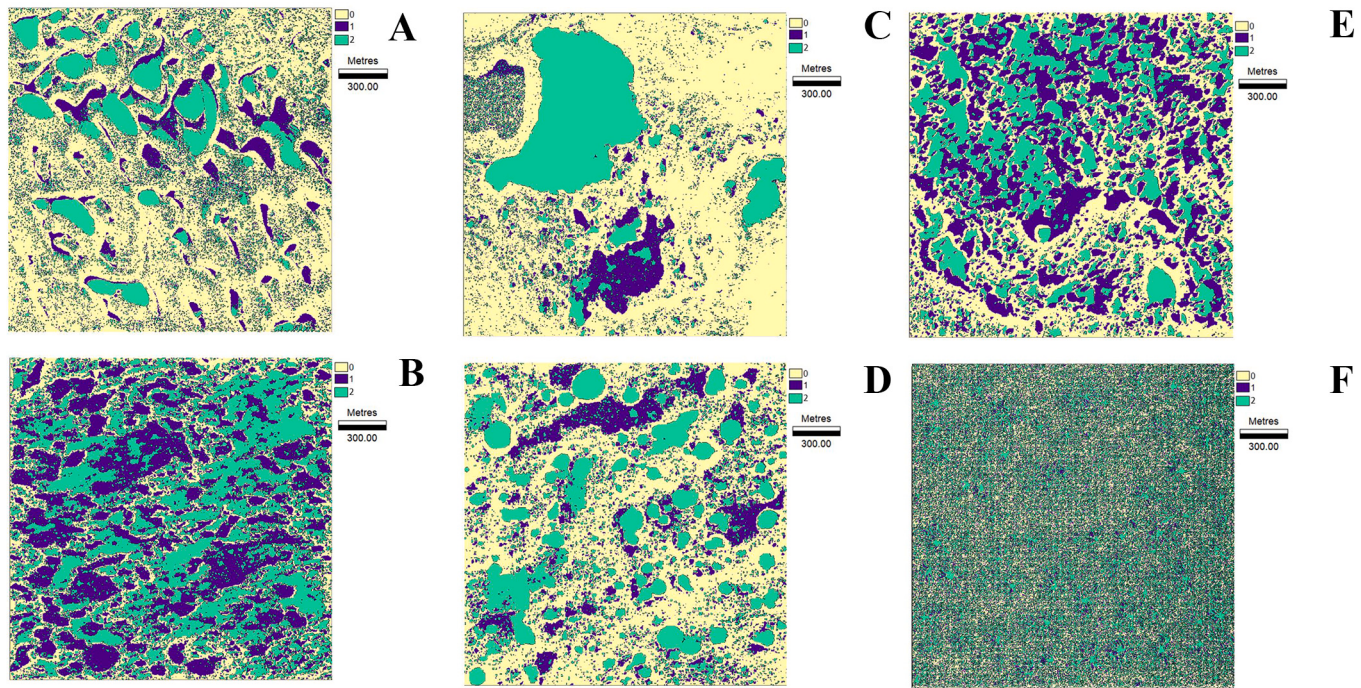


Fig. 19. Maps with joint representation of depressions (2, green) and mounds (1, purple) for aeolian terrain (A), volcanic terrain (B), hydrated terrain (C), cratered terrain (D), reticulate terrain (E) and sublimated terrain (F). (For interpretation of the references to colour in this figure legend, the reader is referred to the web version of this article.)

correlated and the important feature is not the absolute altitude but the relative altitude between pixels. We have found for Earth that 1-pixel depressions are real features in the terrain when using a DEM of quality similar to that of HiRISE DEMs. Furthermore, the number of one-pixel depressions agrees with the number predicted by fractal size-distribution theory and fractal extrapolation. Fig. 21 shows a log-log plot of an area of depressions (in pixels) and the number of mapped depressions (solid colour dots) where the surface (in pixels) is larger than the area. The experimental data follow a straight line which implies a power-law size-distribution. Thus, a power-law has been fitted to each test site and the equations are shown in the figure for each terrain type. These fitted power laws allow fractal extrapolation in order to find the expected number of 1-pixel depressions according to the fractal theory implied in the fitting of the power law. The number of 1-pixel depressions are shown in Table 5 from which it can be seen that the number of 1-pixel mapped depressions is less than the number of 1-pixel depressions predicted by extrapolation from fractal theory. Thus, in specific applications they can be either be treated as real features or they can be deleted by the planetary geologist. In any case, why is there a deficit of small depressions? The answer is that it is due to nested depressions.

Inside the large, mapped depressions there are small depressions that have not been mapped as individual small depressions because they are hidden within the bathymetry of the large depressions. They could be identified and delineated if the DEM does not completely cover the large depression (i.e., the large depression is not closed inside the local DEM). In this case we can apply the methodology proposed in this paper. Thus, for example, in the sublimated terrain where there are no large depressions, the number of 1-pixel mapped depressions is closer to the fractal predicted number. In summary, the full maps with 1-cell

depressions included can be considered or they can easily be filtered to retain only the depressions larger than a given threshold.

5. Conclusions

With respect to previously published work, the novelty of this paper is the metric spatial-scale mapping of closed terrain depressions on Mars and the introduction of the mapping of mounds on Martian landscapes at the metric spatial-scale. A non-exhaustive but representative selection of six landscape terrains (aeolian, volcanic, hydrated, cratered, reticulate and sublimated) are considered and compared. Metric spatial-scale depressions and mounds are ubiquitous in any Martian landscape with a density as high as 296 closed depressions and 278 mounds per hectare for sublimated terrain. This is the more balanced terrain with araneiform geomorphology in which the ‘legs’ of the spiders are elongated depressions carved by the sublimation of the CO₂ ice cap and removal of the material that forms the complementary elongated mounds. Globally, two groups of geomorphologies have been identified. The first is a detached geomorphology formed in terrains where there is detached material, such as sand in aeolian terrain and dry ice in sublimated terrain, which has a plastic behaviour; hydrated terrain is also included in this group. The second group is formed by volcanic, cratered and reticulate terrains in which it appears that the depressions are mounds on the bedrock forming a continuous (i.e., non-detached) geomorphology with the bedrock and the depressions and mounds are formed by volcanic and tectonic processes as well as impact cratering. The analysis of the aeolian terrain has identified blowouts and their associated pan marginal lunette dunes. The analysis of the volcanic terrain suggests that, in this type of terrain, the closed depressions and mounds are mainly erosion-transformed depressions and mounds. The analysis of the hydrated

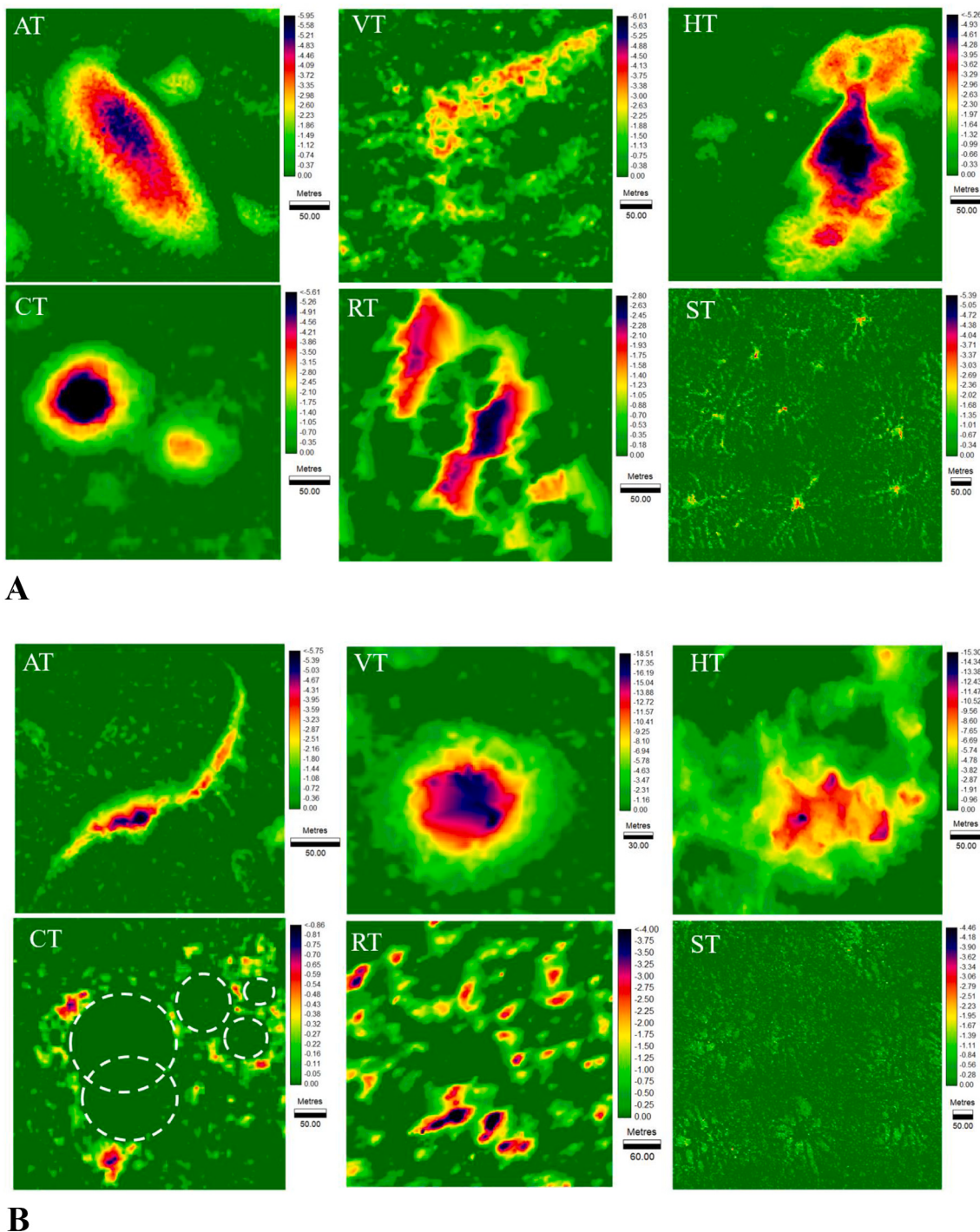


Fig. 20. A. Typical depressions in aeolian terrain (AT), volcanic terrain (VT), hydrated terrain (HT), cratered terrain (CT), reticulate terrain (RT) and sublimated terrain (ST). B. Typical mounds in aeolian terrain (AT), volcanic terrain (VT), hydrated terrain (HT), cratered terrain (CT), reticulate terrain (RT) and sublimated terrain (ST). The mound in the aeolian terrain is a pan margin lunette dune, the mound in the volcanic terrain corresponds to a small volcanic dome, the mounds in the cratered terrain correspond to the ejected material from impact craters.

terrain is consistent with that of an evaporite karst. The analysis of the cratered terrain seems to reflect the typical impact crater landscape, perhaps on icy ground. The analysis of the reticulated terrain shows a jigsaw puzzle pattern of depressions and mounds possibly of polygenic origin. Finally, the analysis of the sublimated terrain has shown a dendritic network of depressions (the legs of the spiders) compensated by mounds.

Notwithstanding the value of these findings, the real benefit of the methodology presented here is that it will provide planetary geologists

with maps of depressions and mounds as additional layers of information in particular, specific and exhaustive studies. The information provided by the analyses shown in this work will contribute to the understanding of the geology and geomorphology of Mars.

Declaration of Competing Interest

None.

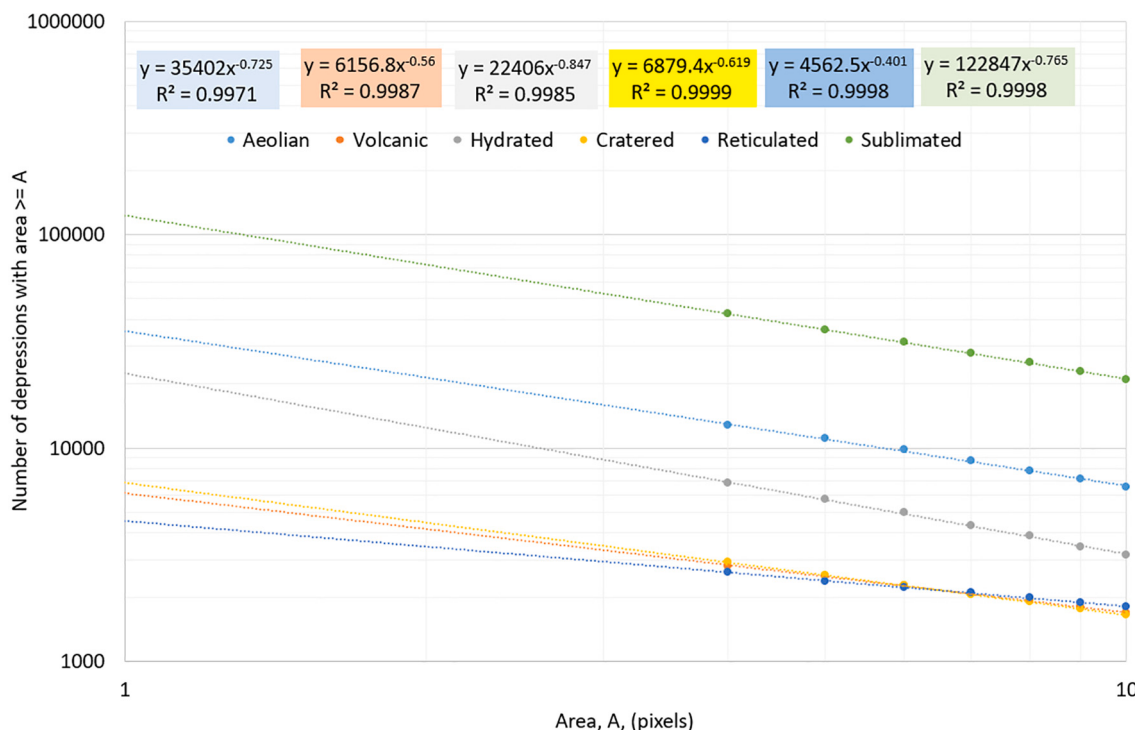


Fig. 21. Log-log plot of an area of depressions (in pixels) and the number of mapped depressions (solid colour dots) in which the surface (in pixels) is larger than the area of the depressions. The coloured dotted lines represent the best power law size-distribution fitted to the mapped depressions for each test site. These fitted power laws allow fractal extrapolation in order to find the expected number of 1-pixel depressions according to the fractal theory implied by the fitted power law. The numbers of 1-pixel depressions are shown in Table 5.

Table 5

1-pixel depressions predicted by fractal extrapolation (Fig. 21) together with actually mapped 1-pixel depressions. All the DEMs have a spatial resolution of 1 m except those marked with an asterisk (*), which have a spatial resolution of 2 m.

| Terrain type (test sites) | Number of 1-pixel depressions from fractal theory | Number of 1-pixel mapped depressions |
|---------------------------|---------------------------------------------------|--------------------------------------|
| Aeolian terrain | 13,969 | 4548 |
| Volcanic terrain (*) | 1980 | 812 |
| Hydrated terrain | 9949 | 3462 |
| Cratered terrain (*) | 2400 | 688 |
| Reticulated terrain | 1107 | 621 |
| Sublimated terrain | 50,557 | 44,976 |

Acknowledgements

This work was supported by research project PID2019-106435GB-I00 of the Ministerio de Ciencia e Innovación of Spain. The contribution of the second author was supported by the Australian Research Council ITTC grant IC190100017. We thank Francesco Mazzarini and two anonymous reviewers by their constructive criticism that has helped us to improve the final version of this paper.

References

- Anderson, R.B., Bell III, J.F., 2010. Geologic mapping and characterization of gale crater and implications for its potential as a mars science laboratory landing site. *Mars* 5, 76–128.
- Arnold, N., 2010. A new approach for dealing with depressions in digital elevation models when calculating flow accumulation values. *Prog. Phys. Geogr.* 34 (6), 781–809.
- Baioni, D., Wezel, F.C., 2010. Morphology and origin of an evaporitic dome in the eastern Tithonium Chasma, Mars. *Planet. Space Sci.* 58, 847–857.
- Baioni, D., Zupan Hajna, N., Wezel, F.C., 2009. Karst landforms in a Martian evaporitic dome. *Acta Carsol.* 38 (1), 9–18.
- Baioni, D., Tramontana, M., Zupan, Hajna N., 2017. Karst landforms within Noctis Labyrinthus, Mars. *Acta Carsologica* 46 (1), 73–82.
- Balogh, S.M., Glaze, L.S., Bruno, B.C., 2007. Nearest-neighbor analysis of small features on Mars: applications to tumuli and rootless cones. *J. Geophys. Res.* 112 (E03002), 1–17.
- Banham, S.G., Gupta, S., Rubin, D.M., Watkins, J.A., Sumner, D.Y., Edgett, K.S., Grotzinger, J.P., Lewis, K.W., Edgar, L.A., Stack-Morgan, K.M., Barnes, R., Bell III, J. F., Day, M.D., Ewing, R.C., Lapotre, M.G.A., Stein, N.T., River-Hernandez, F., Vasavada, A.R., 2018. Ancient Martian aeolian processes and palaeomorphology reconstructed from the Stimson formation on the lower slope of Aeolis Mons, Gale crater, Mars. *Sedimentology* 65, 993–1042.
- Barchyn, T.E., Hugenholtz, C.H., 2013. Dune field reactivation from blowouts: sevier Desert, UT, USA. *Aeolian Res.* 11, 75–84.
- Barlow, N.G., Bradley, T.L., 1990. Martian impact craters: correlations of ejecta and interior morphologies with diameter, latitude, and terrain. *Icarus* 87 (1), 156–179.
- Bernhardt, H., Reiss, D., Hiesinger, H., Ivanov, M.A., 2016. The honeycomb terrain on the Hellas basin floor, Mars: a case for salt or ice diapirism. *J. Geophys. Res. Planets* 121, 714–738.
- Bleacher, J.E., Glaze, L.S., Greeley, R., Hauber, E., Baloga, S.M., Sakimoto, S.E.H., Williams, D.A., Glotch, T.D., 2009. Spatial and alignment analyses for a field of small volcanic vents south of Pavonis Mons and implications for the Tharsis province, Mars. *J. Volcanol. Geotherm. Res.* 185, 96–102.
- Bosák, P., Bruthans, J., Filippi, M., Svoboda, T., Šmid, J., 1999. Karst and caves in salt diapirs, SE Zagros Mts. (Iran). *Acta Carsologica* 28 (2), 41–75.
- Bridges, N.T., Geissler, P.E., McEwan, A.S., Thomson, B.J., Chuang, F.C., Herkenhoff, K. E., Keszthelyi, L.P., Martínez-Alonso, S., 2007. Windy Mars: a dynamic planet as seen by the HiRISE camera. *Geophys. Res. Lett.* 34 (L23205), 1–7.
- Bridges, N.T., Banks, M.E., Beyer, R.A., Chuang, F.C., Noe Dobre, E.Z., Herkenhoff, K.E., Keszthelyi, L.P., Fishbaugh, K.E., McEwan, A.S., Michaels, T.I., Thomson, B.J., Wray, J.J., 2010. Aeolian bedforms, yardangs, and indurated surfaces in the Tharsis Montes as seen by the HiRISE camera: evidence for dust aggregates. *Icarus* 205, 165–182.
- Brock-Hon, A., Hon, K., McCarragher, S., 2019. Geomorphic and geophysical evidence of a collapse origin for large sandstone depressions atop the western Cumberland plateau in Tennessee. *Geomorphology* 343, 168–182.
- Brož, P., Hauber, E., 2012. A unique volcanic field in Tharsis, Mars: pyroclastic cones as evidence for explosive eruptions. *Icarus* 218 (1), 88–99.
- Brož, P., Čadek, O., Hauber, E., Rossi, A.P., 2014. Shape of scoria cones on Mars: insights from numerical modeling of ballistic pathways. *Earth Planet. Sci. Lett.* 406, 14–23.

- Brož, P., Čadek, O., Hauber, E., Rossi, A.P., 2015. Scoria cones on Mars: detailed investigation of morphology based on high-resolution digital elevation models. *J. Geophys. Res. Planets* 120, 1512–1527.
- Brož, P., Fawdon, P., Čadek, O., 2017. Kilometer-sized cones on Mars: igneous or mud volcanoes? *Lunar Plan. Sci. Conf.* No. 1964.
- Brož, P., Hauber, E., van de Burgt, I., Špíller, V., Michael, G., 2019. Subsurface sediment mobilization in the southern Chryse Planitia on Mars. *J. Geophys. Res. Planets* 124 (3), 703–720.
- Bruno, B.C., Fagents, S.A., Hamilton, C.W., Burr, D.M., Baloga, S.M., 2006. Identification of volcanic rootless cones, ice mounds, and impact craters on Earth and Mars: using spatial distribution as a remote sensing tool. *J. Geophys. Res.* 111 (E06017), 1–16.
- Buczkowski, D.L., 2007. Stealth quasi-circular depressions (sQCD) in the northern lowlands of Mars. *J. Geophys. Res.* 112 (E09002), 1–19.
- Carr, M.H., 2001. Mars global surveyor observations of Martian fretted terrain. *J. Geophys. Res.* 106 (E10), 23571–23593.
- Chojnacki, M., Moersch, J.E., Burr, D.M., 2010. Climbing and falling dunes in Valles Marineris. *Mars. Geophys. Res. Lett.* 37 (L08201), 1–7.
- Clark Labs, 2000. The Idrisi Project. 950 Main Street, Worcester MA 01610-1477 USA. <https://clarklabs.org>.
- Conrad, O., Bechtel, B., Bock, M., Dietrich, H., Fischer, E., Gerlitz, L., Wehberg, J., Wichmann, V., Böhner, J., 2015. System for automated geoscientific analyses (SAGA) v. 2.1.3. *Geosci. Model Dev.* 8 (7), 1991–2007.
- Dapremont, A.M., Wray, J.J., 2021. Igneous or mud volcanism on Mars? The case study of Hephaestus Fossae. *J. Geophys. Res. Planets* 126 (2), e2020JE006390.
- Daubar, J.I., McEwen, A.S., Byrne, S., Kennedy, M.R., Inanov, B., 2013. The current martian cratering rate. *Icarus* 225 (1), 506–516.
- Davis, P.A., Tanaka, K.L., Golombok, M.P., 1995. Topography of closed depressions, scarps, and grabens in the north Tharsis region of Mars: implications for shallow crustal discontinuities and graben formation. *Icarus* 114 (2), 403–422.
- De Toffoli, B., Pozzobon, R., Mazzarini, F., Orgel, C., Massironi, M., Giacomini, L., Mangold, N., Cremonese, G., 2018. Estimate of depths of source fluids related to mound fields on Mars. *Planet. Space Sci.* 164, 164–173.
- De Toffoli, B., Pozzobon, R., Massironi, M., Mazzarini, F., Conway, S., Cremonese, G., 2019. Surface expressions of subsurface sediment mobilization rooted into a gas hydrate-rich cryosphere on Mars. *Sci. Rep.* 9 (8603), 1–9.
- de Villiers, S., Nermoën, A., Jamteveit, B., Mathiesen, J., Meakin, P., Werner, S.C., 2012. Formation of Martian araneiforms by gas-driven erosion of granular material. *Geophys. Res. Lett.* 39 (L13204), 1–5.
- Diniega, S., Sangha, S., Browne, B., 2018. Using satellite imagery to identify and analyze tumuli on Earth and Mars. *Earth Planet. Sci. Lett.* 482, 52–61.
- Dodds, P.S., Rothman, D.H., 2000. Scaling, universality, and geomorphology. *Annu. Rev. Earth Planet. Sci.* 28, 571–610.
- Dundas, C.M., Byrne, S., McEwen, A.S., 2015. Modeling the development of martian sublimation thermokarst landforms. *Icarus* 262, 154–169.
- Edgar, L.A., Skinner, J.A., Fortezzo, C.M., Bennett, K.A., 2019. Geologic Mapping and Stratigraphic Analyses in South-Western Melas Chasma. *Planetary Geologic Mappers 2019 (LPI Contribution number 2154)*, 7018.pdf, pp. 1–2.
- ESRI, 2011. ArcGIS Desktop: Release 10. Environmental Systems Research Institute, Redlands, CA.
- Essefi, E., Komatsu, G., Fairén, A.G., Chan, M.A., Yaich, C., 2014. Models of formation and activity of spring mounds in the Mechertate-Chrita-Sidi El Hani system, eastern Tunisia: implications for the habitability of Mars. *Life* 4, 386–432.
- Farrand, W.H., Gaddis, L.R., Keszthelyi, L., 2005. Pitted cones and domes on Mars: observations in Acidalia Planitia and Cydonia Mensae using MOC, THEMIS, and TES data. *J. Geophys. Res. Planets* 110 (E05005), 1–14.
- Ferreira, H., Boulet, R., 1996. Evolution and opening of closed depressions developed in a quartz-kaolinitic sedimentary substratum at Taubaté basin (São Paulo, Brazil), and analogy to the slope evolution. *Geomorphology* 16 (1), 77–86.
- Gendrin, A., Mangold, N., Bibring, J.-P., Langevin, Y., Gondet, B., Poulet, F., Bonello, G., Quantin, C., Mustard, J., Arvidson, R., LeMouélic, S., 2005. Sulfates in Martian layered terrains: the OMEGA/Mars express view. *Science* 307, 1587–1591.
- Gillijns, K., Poesen, J., Deckers, J., 2005. On the characteristics and origin of closed depressions in loess-derived soils in Europe—a case study from Central Belgium. *CATENA* 60 (1), 43–58.
- Graettinger, A.H., Hughes, C.G., Clarke, D.V., Banes, A., Sewell, K., 2017. Holey Mars: distinguishing between small depressions on the surface of Mars. *Lunar Planet. Sci. XLVIII*, 1112.Pdf.
- Graf, J.E., Zurek, R.W., Eisen, H.J., Jai, B., Johnston, M.D., DePaula, R., 2005. The Mars reconnaissance orbiter Mission. *Acta Astron.* 57 (2–8), 566–578.
- Gustavson, T.C., Smpkins, W.W., Alhades, A., Hoadley, A., 1982. Evaporite dissolution and development of karst features on the rolling plains of the Texas panhandle. *Earth Surf. Process. Landf.* 7 (6), 545–563.
- Hallet, B., 1990. Spatial self-organization in geomorphology: from periodic bedforms and patterned ground to scale-invariant topography. *Earth Sci. Rev.* 29 (1–4), 57–75.
- Hao, J., Michael, G.G., Adeli, S., Jaumann, R., 2019. Araneiform terrain formation in Angustus Labyrinthus, Mars. *Icarus* 317, 479–490.
- Hemmi, R., Miyamoto, H., 2018. High-resolution topographic analyses of mounds in southern Acidalia Planitia, Mars: implications for possible mud volcanism in submarine and subaerial environments. *Geosciences* 8 (5). <https://doi.org/10.3390/geosciences8050152>.
- Hepburn, A.J., Holt, T., Hubbard, B., Ng, F., 2019. Creating HiRISE Digital Elevation Models for Mars Using the Open-Source Ames Stereo Pipeline Geoscientific Instrumentation Methods and Data Systems. <https://doi.org/10.5194/gi-2019-11>.
- Hiesinger, H., Head III, J.W., 2003. The Syrtis Major volcanic province, Mars: synthesis from Mars global surveyor data. *J. Geophys. Res.* 109 (E01004), 1–37.
- Hobbs, S.W., Paull, D.J., Bourke, M.C., 2010. Aeolian processes and dune morphology in Gale crater. *Icarus* 210, 102–115.
- Hudec, M.R., Jackson, M.P.A., 2007. Terra infirma: understanding salt tectonics. *Earth Sci. Rev.* 82, 1–28.
- Hynek, B.M., Phillips, R.J., Arvidson, R.E., 2003. Explosive volcanism in the Tharsis region: global evidence in the Martian geologic record. *J. Geophys. Res.* 108 (E9), 1–16, 5111.
- Jeanpert, J., Genton, P., Maurizot, P., Folio, J.-L., Vendé-Leclerc, M., Sérino, J., Join, J.-L., Iseppi, M., 2016. Morphology and distribution of dolines on ultramafic rocks from airborne LiDAR data: the case of southern Grande Terre in New Caledonia (SW Pacific). *Earth Surf. Process. Landf.* 41 (13), 1854–1868.
- Jenson, S.K., 1991. Applications of hydrologic information automatically extracted from digital elevation models. *Hydrol. Process.* 5 (1), 31–44.
- Jenson, S.K., Domingue, J.O., 1988. Extracting topographic structure from digital elevation data for geographic information system analysis. *Photogramm. Eng. Remote. Sens.* 54 (11), 1593–1600.
- Jin, S., Zhang, T., 2014. Automatic detection of impact craters on Mars using a modified adaboosting method. *Planet. Space Sci.* 99, 12–117.
- Karátson, D., Thouret, J.-C., Moriya, I., Lemoschitz, A., 1999. Erosion calderas: origins, processes, structural and climatic control. *Bull. Volcanol.* 61, 174–193.
- Kieffer, H.H., 2000. Annual punctuated CO₂ slab-ice and jets on Mars. In: Mars Polar Science Conference, p. #4095.
- Kim, J.-R., Lin, S.-Y., Müller, J.-P., Warner, N.H., Gupta, S., 2013. Multi-resolution digital terrain models and their potential for Mars landing site assessments. *Planet. Space Sci.* 85, 89–105.
- Kirk, R.L., Howington-Kraus, E., Rosiek, M.R., Anderson, J.A., Archinal, B.A., Becker, K.J., Cook, D.A., Galuszka, D.M., Geissler, P.E., Hare, T.M., Holmberg, I.M., Keszthelyi, L.P., Redding, B.L., Delamere, W.A., Gallagher, D., Chapel, J.D., Elias, E.M., King, R., McEwen, A.S., 2008. Ultrahigh resolution topographic mapping of Mars with MRO HiRISE stereo images: meter-scale slopes of candidate Phoenix landing sites. *J. Geophys. Res.* 113 (E00A24), 1–31.
- Kite, E.S., Sneed, J., Mayer, D.P., Lewis, K.W., Michaels, T.L., Hore, A., Rafkin, C.R., 2016. Evolution of major sedimentary mounds on Mars: buildup via anticompen-sational stacking modulated by climate change. *J. Geophys. Res. Planets* 121, 2282–2324.
- Klimchouk, A., Forti, P., Cooper, A., 1996. Gypsum karst of the world: a brief overview. *Int. J. Speleol.* 25 (3–4), 159–180.
- Komatsu, G., Okubo, C.H., Wray, J.J., Ojha, L., Cardinale, M., Murana, A., Orosei, R., Chan, M.A., Ormrod, J., Gallagher, R., 2016. Small edifice features in Chryse Planitia, Mars: assessment of a mud volcano hypothesis. *Icarus* 268, 56–75.
- Launspach, J., 2013. Automated Sinkhole Extraction and Morphological Analysis in Northeast Iowa Using High-Resolution LiDAR Data. MS Thesis. University of Northern Iowa, p. 104.
- Lawson, M.P., Thomas, D.S.G., 2002. Late quaternary lunette dune sedimentation in the southwestern Kalahari desert, South Africa: luminescence based chronologies of aeolian activity. *Quat. Sci. Rev.* 21, 825–836.
- Le Corvec, N., Spörl, K.B., Rowland, J., Lindsay, J., 2013. Spatial distribution and alignments of volcanic centers: clues to the formation of monogenetic volcanic fields. *Earth Sci. Rev.* 124, 96–114.
- Levy, J.S., Goudge, T.A., Head, J.W., Fassett, C.I., 2017. Candidate volcanic and impact-induced ice depressions on Mars. *Icarus* 285, 185–194.
- Lezama, J., Randall, G., Morel, J.-M., von Gioi, R.G., 2015. An unsupervised point alignment detection algorithm. *IPOL Image Processing On Line* 5, 296–310.
- Liu, Z., Dong, Z., Cui, X., 2018. Morphometry of lunette dunes in the Tirari Desert, South Australia. *Open Geosci.* 10, 452–460.
- Mazzarini, F., D’Orazio, M., 2003. Spatial distribution of cones and satellite-detected lineaments in the Pali Aike volcanic field (southernmost Patagonia): insights into the tectonic setting of a Neogene rift system. *J. Volcanol. Geotherm. Res.* 125, 291–305.
- Mazzarini, F., Isola, I., 2021. Vent distribution and structural inheritance in an embryonic rift: the example of the Chyulu Hills off-rift magmatic range (South Kenya). *J. Volcanol. Geotherm. Res.* 416 (107268), 1–18.
- McCauley, J.F., 1973. Mariner 9 evidence for wind erosion in the equatorial and mid-latitude regions of Mars. *J. Geophys. Res.* 78 (20), 4123–4137.
- McEwen, A.S., Banks, M.E., Baugh, N., Becker, K., Boyd, A., Bergstrom, J.W., Beyer, R.A., Bortolini, E., Bridges, N.T., Byrne, S., 61 More coauthors, 2010. The high resolution imaging science experiment (HiRISE) during MRO’s primary science phase (PSP). *Icarus* 205 (81), 2–37.
- Noe Dobre, E.Z., Asphaug, E., Grant, J.A., Kessler, M.A., Mellon, M.T., 2007. Patterned ground as an alternative explanation for the formation of brain coral textures in the mid latitudes of Mars: HiRISE observations of lineated valley fill textures. In: Seventh International Conference on Mars, California Institute of Technology, Pasadena, California, United States, 3358.Pdf, pp. 1–4.
- Oehler, D.Z., Allen, C.C., 2010. Evidence for pervasive mud volcanism in Acidalia Planitia, Mars. *Icarus* 208, 636–657.
- Oehler, D.Z., Allen, C.C., 2012. Giant Polygons and Mounds in the Lowlands of Mars: Signatures of an Ancient Ocean? *Astrobiology* 12 (6), 601–615.
- Pardo-Igúzquiza, E., Dowd, P.A., 2020a. Identification and delineation of the Earth’s large-scale closed terrain depressions and their fractal size distribution. *Math. Geosci.* <https://doi.org/10.1007/s11004-020-09888-9>.
- Pardo-Igúzquiza, E., Dowd, P.A., 2020b. Identification, delineation and morphometric analysis of closed terrain depressions on Mars. *Icarus* 348, 113869.
- Pardo-Igúzquiza, E., Durán, J.J., Dowd, P.A., 2013. Automatic detection and delineation of karst terrain depressions and its application in geomorphological mapping and morphometric analysis. *Acta Carsologica* 42 (1), 17–24.
- Pardo-Igúzquiza, E., Durán, J.J., Luque-Espinar, J.A., Martos-Rosillo, S., 2014. Analysis of karst terrains using the digital elevation model. Application to the Sierra de las Nieves (Province of Málaga). *Bol. Geol. Min.* 125 (3), 381–389.

- Pardo-Igúzquiza, E., Pulido-Bosch, A., López-Chicano, M., Durán, J.J., 2016. Morphometric analysis of karst depressions on a Mediterránea karst massif. *Geogr. Ann. Ser. A Phys. Geogr.* 98 (3), 247–263.
- Pardo-Igúzquiza, E., Dowd, P.A., Durán, J.J., Robledo-Ardila, P., 2019. A review of fractals in karst. *Int. J. Speleol.* 48, 11–20.
- Parenti, C., Gutiérrez, F., Baioni, D., García-Arnay, A., Sevil, J., Luzzi, E., 2020. Closed depressions in Kotido crater, Arabia Terra, Mars: Possible evidence of evaporite dissolution-induced subsidence. *Icarus* 341, 113680.
- Phillips, C.B., Burr, D.M., Beyer, R.A., 2007. Mass movement within a slope streak on mars. *Geophys. Res. Lett.* 34 (L21202), 1–5.
- Piqueux, S., Byrne, S., Richardson, M.I., 2003. Sublimation of Mars's southern seasonal CO₂ ice cap and the formation of spiders. *J. Geophys. Res.* 108 (E8), 5084, 1–9.
- Planchon, O., Darboux, F., 2001. A fast, simple and versatile algorithm to fill the depressions of digital elevation models. *Catena* 46, 159–176.
- Pondrelli, M., Rossi, A.P., Ori, G.G., van Gasselt, S., Praeg, D., Ceramicola, S., 2011. Mud volcanoes in the geologic record of mars: the case of Firsoff crater. *Earth Planet. Sci. Lett.* 304 (3–4), 511–519.
- Pozzobon, R., Mazzarini, F., Massironi, M., Rossi, A.P., Pondrelli, M., Cremonese, G., Marinangeli, L., 2019. Fluids mobilization in Arabia Terra, mars: depth of pressurized reservoir from mounds self-similar clustering. *Icarus* 321, 938–959.
- QGIS Development Team, 2020. QGIS Geographic Information System. Open Source Geospatial Foundation Project. <http://qgis.osgeo.org>.
- Rampey, M.L., Milam, K.A., McSween Jr., H.Y., Moersch, J.E., Christensen, P.R., 2007. Identity and emplacement of domical structures in the western Arcadia Planitia, Mars. *J. Geophys. Res.* 112 (E06011), 1–27.
- Reams, M.W., 1992. Fractal dimensions of sinkholes. *Geomorphology* 5, 159–165.
- Richardson, J.A., Bleacher, J.E., Connor, C.B., Glaze, L.S., 2021. Small volcanic vents of the tharsis volcanic province, mars. *J. Geophys. Res. Plan.* 126 (2), e2020JE006620.
- Rodríguez, J.A.P., Tanaka, K.L., Kargel, J.S., Dohm, J.M., Kuzmin, R., Fairén, A.G., Sasaki, S., Komatsu, G., Schulze-Makuch, D., Jianguo, Y., 2007. Formation and disruption of aquifers in southwestern Chryse Planitia, mars. *Icarus* 191 (2), 545–567.
- Rodríguez, J.A.P., Kargel, J.S., Tanaka, K.L., Crown, D.A., Berman, D.C., Fairén, A.G., Baker, V.R., Furfarò, R., Candelaria, P., Sasaki, S., 2013. Secondary chaotic terrain formation in the higher outflow channels of southern circum-Chryse, mars. *Icarus* 213 (1), 150–194.
- Sauro, U., 2003. Dolines and sinkholes: aspects of evolution and problems of classification. *Acta Carsologica* 32 (2), 41–52.
- Sauro, U., 2019. Solution dolines as the diagnostic forms of karst surfaces. In: White, W., Culver, D., Pipan, T. (Eds.), *Encyclopedia of Caves*, 3rd ed. Elsevier, pp. 140–155.
- Schwamb, M.E., Aye, K.M., Portykina, G., Hansen, C.J., Allen, C., Allen, S., Calef, F.J., Duca, S., McMaster, Miller, G.R.M., 2018. Planet four: terrains – discovery of araneiforms outside of the south polar layered deposits. *Icarus* 308, 148–187.
- Seekell, D.A., Pace, M.L., Tranvik, L.J., Verpoorter, C., 2013. A fractal-based approach to lake size-distributions. *Geophys. Res. Lett.* 40, 517–521.
- Smyth, T.A.G., Hesp, P.A., Walker, I.J., Wasklewicz, T., Gares, P.A., Smith, A.B., 2019. Topographic change and numerically modelled near surface wind flow in a bowl blowout. *Earth Surf. Process. Landf.* 44, 1988–1999.
- Soare, R.J., Conway, S.J., Pearce, G.D., Costard, F., Séjourné, A., 2013. Sub-kilometre (intra-crater) mounds in utopia Planitia. Mars: Character Occurrence and Possible Formation Hypotheses 225 (2), 982–991.
- Spencer, J.R., Fanale, F.P., 1990. New models for the origin of Valles Marineris closed depressions. *J. Geophys. Res.* 95, 14301–14313.
- Stuart, R.J., Hynek, B.M., 2012. A new global database of Mars impact craters ≥ 1 km: 2. Global crater properties and regional variations of the simple-to-complex transition diameter. *J. Geophys. Res. Planets* 117 (E06001), 1–21.
- Stuart, R.J., Hynek, B.M., 2014. The secondary crater population of mars. *Earth Planet. Sci. Lett.* 400, 66–76.
- Tognetti, L.A., 2019. Investigating a Link between Topography and Scalloped Depressions in Utopia Planitia, Mars. Master Thesis. Arizona State University, p. 48.
- Trier, Ø.D., Pilø, L.H., 2012. Automatic detection of pit structures in airborne laser scanning data. *Archaeol. Prospect.* 19 (2), 103–121.
- Viola, D., McEwen, A.S., Dundas, C.M., Byrne, S., 2015. Expanded secondary craters in the Arcadia Planitia region, Mars: evidence for tens of Myr-old shallow subsurface ice. *Icarus* 248, 190–204.
- Wang, L., Liu, H., 2006. An efficient method for identifying and filling surface depressions in digital elevation models or hydrologic analysis and modelling. *Int. J. Geogr. Inf. Sci.* 20, 193–213.
- Watson, A., 1986. The origin and geomorphological significance of closed depressions in the Lubombo Mountains of Swaziland. *Geogr. J.* 152 (1), 65–74.
- Wood, S.E., Paige, D.A., 1992. Modeling the Martian seasonal CO₂ cycle: 1. Fitting the viking lander pressure curves. *Icarus* 99, 1–14.
- Yong-He, Wan-Chang, Z., Jing-Wen, X., 2009. Another fast and simple DEM depression-filling algorithm based on priority queue structure. *Atmosph. Ocean. Sci. Lett.* 2, 214–219.